Structural and electronic properties of small anionic magnesium clusters

Author: *Ainhoa Faustino* and Advisor: *Andrés Aguado*

Departamento de Física Teórica, Atómica y Óptica
Universidad de Valladolid, E-47011 Valladolid, Spain.

Final Master Project

Abstract

The main objective of this Master Degree Work is to analyze the structural and electronic properties of small magnesium cluster anions employing computational techniques, and to reproduce and interpret experimental measurements reported for this physical system. In a first step, we will locate the global minimum structures of Mg_N^- cluster anions wirh $N = 3 - 38$ atoms, by employing first-principles (*ab initio*) computational techniques based on DFT (Density Functional Theory) as a method to solve the electronic problem. Our theoretical stabilities succeed in reproducing the relative cluster abundances measured by mass spectroscopy techniques. Finally, we report a detailed analysis of several electronic indicators (ionization potential, band gap, density of electronic states, etc.), aimed at reproducing experimental photoemission spectra and assessing the evolution of metallic behavior in Mg clusters of increasing size. In general, we conclude that our theoretical results are in good agreement with experimental measurements.

El objetivo de este Trabajo de Fin de Máster consiste en aplicar técnicas de simulación computacional para analizar las propiedades electrónicas y estructurales de pequeños agregados aniónicos de magnesio, intentando reproducir e interpretar físicamente medidas experimentales realizadas previamente sobre dicho sistema. Para ello, obtendremos en un primer paso las estructuras de mínima energía de agregados Mg_N^- con $N = 3 - 38$ átomos, utilizando un método de primeros principios (*ab initio*) basado en la Teoría del Funcional de la Densidad (DFT, por "Density Functional Theory") para resolver el problema electrónico. Con las energías calculadas, se consigue reproducir e interpretar las abundancias relativas de estos agregados, medidas en espectros de masas. Finalmente, ofreceremos un análisis de diversas propiedades electrónicas (potencial de ionización, salto de banda, densidad de estados electrónicos, etc.) con el objetivo de estudiar el comportamiento metálico de estos agregados e interpretar espectros foto-electrónicos publicados en trabajos previos. En general, observamos un muy buen acuerdo con los resultados experimentales disponibles.

keywords : Density functional theory, anionic, magnesium, clusters

---

I Introduction

Over the last decades, nanomaterials have been one of the fastest-growing technological areas in Materials Science due to the development of nanoscience. At this length scale, the quantum mechanical effects dominate over classical ones, causing the nanoparticles to have different properties from those of the macroscopic world. Moreover, those properties are strongly size-dependent and vary drastically upon adding or removing one atom from the nanoparticle, making it difficult to predict its physico-chemical behavior. Hence an understanding of the properties of isolated (free-standing) clusters is an essential first step towards contolled manipulation of new materials and development of technological devices for particular applications.

Atomic clusters are particles composed by a countable number of atoms [1], ranging from two in the diatomic molecule to several hundred thousand atoms. In this size range, the geometric and electronic structures are the most fundamental properties of clusters to control and optimize, for instance, catalytic activities or electronic, optical and magnetic responses; often these properties are unrelated to those of the corresponding bulk material.

Among the systems that have attracted substantial interest in the last years, there are clusters of divalent metallic elements where the two valence electrons occupy the $s-$orbital, and where the next empty $p-$orbital is well separated by an energy gap. In the bulk limit, these materials are metallic, hence upon increasing the number of atoms a transition must occur from non-metallic to metallic bonding [2], [3] [4], [5], [6].

In my previous work, reported as a final degree project[7], we considered both neutral and charged magnesium clusters with up to $N = 21$ atoms. Continuing with that line of research, in this work we will focus on structural and electronic properties of negatively singly-charged Mg_N^- clusters with $N = 3 - 38$ atoms. There are at least two reasons for considering only anions now: (1) the computational expense of the calculations increases very fast with system size, but most importantly (2) there are more experimental results available for anions in the literature.

A fundamental characteristic of these divalent metal clusters is that certain sizes form preferentially, i.e. are more abundant, in the experimental mass spectra. Some clusters have a higher stability than others because they possess special numbers of electrons, known as "magic numbers" [8].

Computer modelling is an essential tool to perform precise simulations and understand why selected numbers of atoms yield enhanced stability in a cluster. Our calculations have been performed using the first-principles software called SIESTA (Spanish Initiative for Electronic Simulations with Thousands of Atoms) **SIESTA**; this code is used for electronic-structure calculations and materials modelling at the nanoscale and it is based on the *Density Functional Theory* (DFT) formalism[9]. It is within this theoretical framework that the global minimum (GM) structures are found. Our results allow studying the evolution of both electronic and geometrical structures, as well as the emergence of metallic behaviour, as a function of the size of the nanoparticle. The stability of a cluster includes contributions from different electronic and geometric factors that have to be investigated. Moreover, an explicit comparison of the theoretical stability trends with the experimental abundances determined by mass spectrometry, and of the theoretical electronic properties with photoemission spectra, will serve to assess the accuracy of the calculations, and so of the conclusions extracted from them.

In particular, magnesium clusters are considered to constitute a paradigmatic system to study the insulator-to-metal transition. As we said above, magnesium is metallic in the bulk limit due to the energy overlap between the electronic bands arising from $s-$ and $p-$ atomic orbitals, i.e. due to a significant $s-p$ hybridization. Thus, we expect that both the $s-p$ hybridization degree and the electron

delocalisation increase with cluster size, and it is a fundamentally interesting issue to know if this evolution towards metallicity is gradual or abrupt, and at which cluster size has the bonding become "metallic-like" [2] [3] [4], [5], [6]. We have focused on addressing this issue as well as other properties of interest to the field of nanoscience.

This work aims at offering a self-contained exposition of the most fundamental properties of magnesium cluster anions. To offer a thorough discussion, this article is structured as follows: in Section II, we will briefly present the theoretical model used to describe the cluster systems at the atomic level. In section III, the description of the computational model used to locate the GM structures is offered. Section IV will be divided into four subsections: the first one (IV. 1.) reports the GM structures of Mg_N^- clusters, describing how their molecular architecture changes with the size of the nanoparticle; secondly, in IV. 2., we compare our theoretical stabilities with the abundance results measured in cluster beam experiments; third, the IV. 3. subsection covers the description of properties which refer to electronic stability; next, subsection IV. 4. adresses the evolution towards metallicity in magnesium clusters as a function of increasing size. Finally, the relevant conclusions that have been reached are shown in section V, emphasizing the importance of fundamental research on metal clusters to the world of nanotechnology.

II Theoretical model

In order to explain the theoretical framework employed to describe our physical system, as well as the conditions of the simulation, let us concentrate first on the fundamental object that governs the physical properties of a cluster at the microscopic level, namely the quantum hamiltonian for a system of electrons and nuclei interacting through the Coulomb force law. In this work we have opted for *first principles* or *ab initio* methods to self-consistently solve the multi-electronic non-relativistic Hamiltonian within an independent-particle mathematical framework. In variational methods of the type here employed, the total energy of a Mg_N^- cluster is then calculated as the expectation value of the exact hamiltonian over a single-determinant approximate electronic ground state wave function. We will see in detail how these methods provide accurate energies at a moderate computational cost.

1 Hamiltonian

A theoretical understanding of the properties of a material system with $N = N_e + N_n$ particles, including N_e electrons and N_n nuclei, resides in its wave function Ψ. In fact, the quantum state of the system is determined by this wave function of $3(N_e + N_n)$ coordinates. In a conservative system, the eigenfunctions of the Hamiltonian operator are obtained by solving the time-independent Schrödinger equation. The set of eigenfunctions, each with an associated eigenvalue E, are called the "*stationary states*" of the system.

The resolution of that equation is an extremely complex problem, therefore certain approximations are usually considered. The first and most fundamental one is the Born-Oppenheimer (also called adiabatic) approximation, where the atomic nuclei are considered as infinitely slow (i.e. essentially immobile) compared to the much higher speed of the electrons. The disparity between nuclear and electronic velocities is due to the large difference in mass between the two types of particles, so this approximation can alternatively be stated by saying that nuclei are infinitely massive as compared to electrons. This allows decoupling the dynamics of nuclear and electronic variables. Hence for each set of (fixed) nuclear coordinates, the nuclei create an external *static* potential where the electrons move, allowing to define *electronic* stationary states. The dynamics of nuclear coordinates then evolves in the average potential created by the continuous charge distribution of the

electronic stationary states.

Thus, the wave function $\Psi = \chi\psi$ is factored into two parts: the one corresponding to the nuclear problem (χ) has an explicit dependence on nuclear coordinates only; the other one (ψ) represents an electronic stationary state, and has a parametric dependence on nuclear coordinates apart from the obvious explicit dependence on electronic coordinates.

In this study, only the electronic component will be obtained at a quantum level for each given nuclear configuration, and we will consider nuclei as classical point particles. Therefore, from now on we will restrict our attention to the so-called electronic hamiltonian, in which the nuclear kinetic energy term is excluded:

$$H\psi = (T + V_{\text{ext}} + V_{nn} + V_{ee})\psi = E\psi \quad (1)$$

where H is the sum of the electronic kinetic energy T, the electron-electron interaction potential energy V_{ee}, the nuclear repulsion energy V_{nn} and the external potential V_{ext} containing the coulomb attraction between the electrons and the frozen nuclei [1]. This last term, therefore, is the one that provides a differentiating factor between systems, because for each fixed value of N_e, the operators T and V_{ee} are universal, i.e. the same for all multielectronic systems. The nuclear term V_{nn} is a constant during the resolution of the electronic equation, and so produces a mere global shift of the eigenvalues. From now on we will not explicitly include this term in the discussion, but it should be understood that it is always included in the calculations. Once we have focused the problem, now the question is how we are going to precisely solve these equations; for this, we will use the following *ab-initio* method.

[1] The external potential V_{ext} term could also include the interaction with externally applied fields.

2 Density Functional Theory

Although the approximations applied up to this point obviously simplify the original problem, determining the eigenvalues of the electronic Hamiltonian equation (1) is still a tough problem. In the following, we describe one of the methodologies used to overcome such problems efficiently: the Density Functional Theory (DFT)[9], [10]. This is an *ab initio* method for solving the nonrelativistic, time-independent Schrodinger equation.

The main idea of DFT is to transform the Schrödinger equation for the N_e electrons of the system into a simpler variational problem, expressed in terms of the electron density $n(\mathbf{r})$ as the fundamental variable:

$$n(\vec{r}) = N_e \int |\psi(\vec{r}, \vec{r}_2, ..., \vec{r}_{N_e})|^2 \, d\vec{r}_2 ... d\vec{r}_{N_e} \quad (2)$$

According to DFT, any electronic property of the system in its ground state can be completely determined once the electron density $n(\mathbf{r})$ is known. Using $n(\mathbf{r})$ instead of the wave function, the number of spatial variables is reduced from $3N_e$ to 3. Thus, this theory significantly reduces the complexity of the problem and so its computational cost.

2.1 Hohenberg-Kohn theorems

DFT is based on two theorems, first formulated by Hohenberg and Kohn[10], which hold for any system of electrons under the influence of an external potential.

The first Hohenberg–Kohn theorem states that the ground-state electron density uniquely determines the corresponding external potential (V_{ext}) up to an additive constant. Consequently, the external potential, and hence the total energy E and even the multi-electron wavefunction, are functionals of the electron density $n(\mathbf{r})$.

The second Hohenberg–Kohn theorem defines an important mathematical property of the energy functional. It states that the ground-state energy is determined by finding the electron density which minimizes the total energy functional. Knowing the explicit expression of this functional ($E[n(\vec{r})]$) is then enough to variationally determine the ground-state density of the system.

Nevertheless, in order to employ the functional $E[n(\vec{r})]$ within a variational framework, we first require to know its explicit expression in terms of the density. Unfortunately, although DFT shows that the functional exists, it does not provide an explicit expression for it, nor any systematic method to calculate it.

At least some relevant terms in the Hamiltonian can easily be expressed as explicit functionals of the density $n(\vec{r})$. The first one is the external potential energy, describing the interaction of the electrons with the electrostatic potential created by the nuclei ($v_{\text{ext}}(\mathbf{r})$):

$$V_{\text{ext}}[n(\mathbf{r})] = \int d\mathbf{r} v_{\text{ext}}(\mathbf{r}) n(\mathbf{r}) \tag{3}$$

The second one is a part of the electron-electron interaction energy V_{ee}. In fact, this interaction can be split into Hartree energy ($V_H[n(\mathbf{r})]$) and so-called exchange and correlation ($E^0_{xc}[n(\mathbf{r})]$) energy contributions:

$$V_{ee}[n(\mathbf{r})] = V_H[n(\mathbf{r})] + E^0_{xc}[n(\mathbf{r})] \tag{4}$$

The first term in equation (4) is the Hartree energy, expressing the coulomb self-repulsion associated with a classical continuous charge distribution of density $n(\vec{r})$, and is known exactly:

$$V_H[n(\mathbf{r})] = \frac{1}{2} \int d\mathbf{r} d\mathbf{r}' \frac{n(\mathbf{r}) n(\mathbf{r}')}{|\mathbf{r} - \mathbf{r}'|} \tag{5}$$

As for the second term in 4, the exchange and correlation functional ($E^0_{xc}[n(\mathbf{r})]$), it is the correction to the Hartree term due to purely quantum exchange effects and also to many-particle correlation effects associated with the point-like character of the electrons. In contrast to the previous terms, the exact explicit expressions for the functionals $E^0_{xc}[n(\mathbf{r})]$ and $T[n]$ are not known.

We will explain later on how one can resort to approximate functional expressions to get around this problem in practice, but before doing that, we notice that the ground-state energy can be obtained at least at a formal level using implicit functionals of the density. In fact, the energy functional can be written as:

$$\begin{aligned} E[n] &= \min < \psi_n | H | \psi_n > = \\ &= \min < \psi_n | T + V_{ee} + V_{ext} | \psi_n > \end{aligned} \tag{6}$$

where the expectation value of the hamiltonian is minimized over the subset of many-body wavefunctions ψ_n that produce a given density $n(\vec{r})$. Further minimizing this functional with respect to the density $n(\vec{r})$ results in an exact implicit expression for the ground-state energy functional, and as a by-product, at the minimum ψ_n would be the ground-state wavefunction as an implicit functional of the density.

The last minimization is usually reformulated by introducing the universal functional $F[n] = T[n] + V_{ee}[n]$, which is the same for any system with a given number of electrons (N_e):

$$E = \min_n \{F[n] + V_{ext}[n]\} \tag{7}$$

Here it is the universal functional $F[n]$ the one that is not known explicitly. As $F[n]$ can itself be written in terms of a minimization over the subset of many-body wavefunctions that produce a density n, at least $F[n]$ can also be known as an implicit functional of the density. Although useful for the theoretical advance of formal DFT, this is not useful for practical computations.

In summary, both T and E^0_{xc} need to be approximated. The exchange and correlation term is usually of the order of 1% of the total energy, but the kinetic energy term is of the same order of magnitude as the total energy according to the virial theorem. It is thus essential to have a very accurate approximation for the kinetic energy functional. Accordingly, let us concentrate first on methods for evaluating the electronic kinetic energy accurately.

2.2 Kohn-Sham Method

Considering the enormous difficulties faced when trying to derive an accurate $T[n]$ functional, Kohn and Sham [11] proposed an alternative method to accurately evaluate the electronic kinetic energy, avoiding the need for an explicit $T[n]$ functional expression. They express this kinetic energy as a sum of two contributions[11]:

$$T[n] = T_s[n] + T_c[n], \tag{8}$$

where $T_s[n]$ represents the kinetic energy of a fictitious system of non-interacting electrons that has the same density n as the true interacting system. Thus, this equation essentially defines T_c as that part of the kinetic energy due to correlation effects. The important point here is that T_c amounts to approximately 1% of the total kinetic energy value, and due to its meaning, is naturally incorporated as part of a redefined exchange and correlation functional:

$$E_{xc}[n] = T_c[n] + E^0_{xc}[n]. \tag{9}$$

On the other hand, the main $T_s[n]$ contribution can be calculated exactly at the cost of introducing an auxiliary set of monoelectronic orbitals φ_i (the Kohn-Sham orbitals), corresponding to the independent particles of the fictitious non-interacting system. Kohn and Sham demonstrated that these orbitals satisfy the typical equations for independent electrons moving in an effective potential $v_{eff}(\mathbf{r})$. The KS equations, one for each electron i, are:

$$(-\frac{\nabla_i^2}{2} + v_{eff}(\mathbf{r}))\varphi_i(\mathbf{r}) = \varepsilon_i\varphi_i(\mathbf{r}). \tag{10}$$

The first term on the left side is the kinetic energy for non-interacting electrons. Nevertheless, the set of occupied KS orbitals spans the true interacting density:

$$n(\mathbf{r}) = \sum_{i=1}^{N} |\varphi_i(\mathbf{r})|^2 \tag{11}$$

The KS equations are nonlinear because the effective potential depends on the KS orbitals φ_i, so the N_e equations must be solved in a self-consistent process. Starting from an initial electronic density the v_{eff} is calculated and used to solve KS equations to get new orbitals that determine a new density. The process is iterated until self-consistency is achieved when the difference between the incoming and outgoing density is less than some convergence threshold defined by the user.

In summary, Kohn and Sham developed an iterative method to obtain the kinetic energy accurately by solving a set of Schrödinger-like equations (10) for independent particles, incorporating all the many-body effects into an effective mean-field potential detailed in the next section. Notice they did not provide an explicit expression for the functional $T_s[n]$, but only an implicit one via the re-introduction of orbitals into the theory, which certainly increases the computational cost. Nevertheless, nowadays is the only DFT method that can provide accurate results for the kinetic energy of arbitrary systems.

2.3 Effective potential

The KS approach just described allows to partition the total energy functional in a different way:

$$E[n] = T_s[n] + V_H[n] + V_{ext}[n] + E_{xc}[n], \tag{12}$$

where only the last term, representing around 1% of the total energy, is unknown now. Therefore, the exchange-correlation functional must be approximated, and we will discuss some of the most frequently used approximation in the next sections.

Assuming by now that we have an approximate expression for $E_{xc}[n]$, the general principles of DFT instruct us to minimize the energy functional to find the ground state density of the system, with the constraint that the total number of electrons, N_e, is constant:

$$\frac{\delta E[n]}{\delta n(\mathbf{r})} = \frac{\delta T_s[n]}{\delta n(\mathbf{r})} + v_H(\mathbf{r}) + v_{ext}(\mathbf{r}) + v_{xc}(\mathbf{r}) = \mu \tag{13}$$

μ is the Lagrange multiplier associated with the constraint $\int n(\vec{r}) = N_e$, and has a well defined physical meaning as the chemical potential

of the electron gas. $v_H(\mathbf{r})$ and $v_{xc}(\mathbf{r})$ are the Hartree and exchange-correlation potentials, respectively:

$$v_H(\mathbf{r}) = \frac{\delta V_H[n]}{\delta n(\mathbf{r})} = \int d\mathbf{r} \frac{n(\mathbf{r}')}{|\mathbf{r} - \mathbf{r}'|} \tag{14}$$

$$v_{xc}(\mathbf{r}) = \frac{\delta E_{xc}[n]}{\delta n(\mathbf{r})} = \frac{\delta(E^0_{xc}[n] + T_c[n])}{\delta n(\mathbf{r})}. \tag{15}$$

Because of the physical meaning attached to $T_s[n]$, the interacting problem is seen to be equivalent to that of independent electrons moving in the following effective potential:

$$v_{eff}(\mathbf{r}) = v_{ext}(\mathbf{r}) + v_H(\mathbf{r}) + v_{xc}(\mathbf{r}), \tag{16}$$

We have finally reached the expression of effective potential that we were looking for, which is essential for iteratively solving the KS equations. In short, we have an expression where we know exactly Hartree's potential (14) but the exchange and correlation potential (15) has to be approximated.

Notice that we have not provided the complete derivation of KS equations in this section, as we have directly used the density $n(\vec{r})$ as variational parameter for brevity reasons. The derivation would be similar to the one shown here, but the variational functions needed to optimize the energy would be the KS orbitals, and more Lagrange multipliers would be needed to enforce normalization of each separate orbital, as well as orthogonality between the different orbitals. The process would be formally similar to the derivation of Hartree-Fock equations.

2.4 Exchange and correlation functionals

The Kohn-Sham equations (10) are exact in principle for any electron gas under the action of a static external potential, as no fundamental approximations other than the Born-Oppenheimer approximation have yet been made. At a practical level, however, we must approximate the unknown exchange and correlation functional term in (9).

This functional can be naturally divided into correlation (E_c) and exchange (E_x) contributions:

$$E_{xc}[n] = E_x[n] + E_c[n]. \tag{17}$$

The exchange component has a purely quantum origin. Due to the Pauli exclusion principle, parallel spin electrons tend to repel each other at short distances due to their antisymmetric spatial wave function, i.e. due to the indistinguishability effects that impose an antisymmetric quantum state for fermions. E_x represents the associated decrease in the electron-electron coulomb repulsive energy.

Unlike the exchange term, correlation effects (E_c) also exist in the classical world. This term reflects how the coulomb repulsion energy of the electronic system decreases due to the correlated motion of the point-like electrons.

So both exchange and correlation effects tend to stabilize the system by keeping electrons apart, thus creating what is called an exchange-correlation hole around each electron. This "hole" represents a region of space around a given electron where it is highly improbable to find other electrons; in other words, each electron generates a hole of electron density around itself.

Based on this concept, the E_{xc} functional can be reformulated as the energy accounting for the attractive interaction between the electron density n and the hole density n_{xc}:

$$E_{xc}[n] = \frac{1}{2} \int \frac{n(\mathbf{r}) n_{xc}(\mathbf{r}, \mathbf{r}')}{|\ \mathbf{r} - \mathbf{r'}\ |} d\mathbf{r} d\mathbf{r}' \tag{18}$$

where the exchange-correlation hole density ($n_{xc}(\mathbf{r}, \mathbf{r}')$) satisfies the normalisation condition known as the sum rule:

$$\int n_{xc}\left(\mathbf{r}.\mathbf{r}'\right) d\mathbf{r}' = -1. \tag{19}$$

Now that we understand a bit better the physical content of the E_{xc} functional, let's review different approaches to approximate it. There are several choices, and the goal is to choose one that covers the requirements of our problem

without being too expensive at a computational level.

The simplest approximation is called the *Local Density Approximation* (LDA). Within this approach, the contribution of each point of space to the exchange-correlation energy exclusively depends on the value of the electron density at that particular point, and it is in this sense that the approximation is termed *local*. The approach considers a homogeneous electron gas as a reference system for which exact numerical results can be obtained. In a homogeneous electron gas, symmetry imposes a constant value for the exchange-correlation energy density at all spatial positions, which has been numerically tabulated as a function of the (constant) density n. Then, in a LDA calculation on a real (inhomogenous) system, the exchange-correlation energy density at each point $\vec{r}$, where the density is $n(\vec{r})$, is approximated by the energy density of an infinite homogeneous gas with the same density:

$$E_{xc}^{\mathrm{LDA}} = \int d\mathbf{r} n(\mathbf{r}) e_{xc}[n(\mathbf{r})], \qquad (20)$$

where $e_{xc}[n(\mathbf{r})]$ is the exchange-correlation energy per particle in a homogeneous gas of density $n = n(\vec{r})$. This approximation is by definition exact for a system with uniform density, and is reasonable if the density is quasi-homogeneous (i.e. if its deviations from the mean density value are of low amplitude).

In many cases these conditions will not be satisfied, particularly so in finite systems such as atoms or molecules, and in surface regions where the electron density decays exponentially fast. As the LDA conditions are no longer met, the approximation is not expected to be accurate.

Another related approach is the *Local Spin Density Approximation* (LSDA), where the local character of the method is maintained, but an extension of density functionals to spin-polarized systems is allowed. The LSDA thus employs two independent scalar fields to describe the total electron density: $n_\uparrow(\mathbf{r})$ and $n_\downarrow(\mathbf{r})$ for the density contributed by spin-up and spin-down electrons, respectively, and with $n(\mathbf{r}) = n_\uparrow(\mathbf{r}) + n_\downarrow(\mathbf{r})$. The LSDA exchange-correlation energy is written as:

$$E_{xc}^{\mathrm{LSDA}} = \int d\mathbf{r} n(\mathbf{r}) e_{xc}[n_\uparrow(\mathbf{r}), n_\downarrow(\mathbf{r})] \qquad (21)$$

Nevertheless, both LSDA and LDA are not accurate in problems where the system cannot be approximated as locally homogeneous. Hence, systems where density varies abruptly require an improved approach. The so-called Generalized Gradient Approximation (GGA) provides an efficient solution by adding an explicit dependence on the density gradient at each point ($\bigtriangledown n(\vec{r})$):

$$E_{xc}^{GGA}[n] = \int n(\vec{r}) e_{xc}[n(\vec{r}), \bigtriangledown n(\vec{r})] d\vec{r} \qquad (22)$$

For inhomogeneous electron densities, like those of molecules, the GGA provides more accurate results. Moreover, for systems with spin polarization, the extension is simply as direct as in LDA, and is the one that will be applied in the simulations performed in this work. In particular, we will employ the specific GGA proposed in 1996 by Perdew, Burke and Ernzerhof, called PBE functional in the literature [10].

2.5 Pseudopotentials

In this section we describe the explicit expression for V_{ext} employed in our calculations, which is obtained from pseudopotential (PP) theory.

In the exposition of DFT that we have made up to this point, the density ($n(\mathbf{r})$) is generated by all the electrons in the system, and the external potential is produced exclusively by nuclei. This type of calculation is called an all-electron (AE) calculation in the literature, and a common feature of AE calculations is that they demand a huge computational cost for large molecules. In this work, which aims to find a good compromise between accuracy and computational expense, we will rather use a so-called pseudopotential approximation, which has the virtue of being much less expensive and almost as accurate as the AE calculations for

the specific purposes of our work.

The electronic structure of an atom is quite naturally divided into valence and core electrons, and the use of all the electrons in a molecular calculation is usually not necessary. Core electrons occupy deep atomic orbitals grouped in closed shells and they do not actively participate in the formation of chemical bonding under normal circumstances. To excite core electrons, one needs rather extreme environmental conditions such as incident photons with very high energies, or application of a huge pressure, so they remain inert in almost all situations of interest in chemistry, which makes it reasonable not to incorporate these electrons actively in the variational optimization. Taking advantage of the inactive character of the core electron states, we have implemented the approximation of considering them part of the external static potential V_{ext}, i.e. to treat them on an equal footing with the nuclei.

The great majority of atoms has more electrons in the core than in the valence shell, so large computational savings result when modelling the atoms in a molecule as having only those electrons that are directly involved in chemical bonding. In this new outline, we will continue to use $n(\vec{r})$ to refer to the density generated by the N_e active valence electrons, so that this "valence density" continues to integrate to the total number of "valence electrons".

The first step is, therefore, to decide which electrons should be considered as frozen in the core and which ones are included in the active valence space; in our case, we will include the $1s^2 2s^2 2p^6$ electrons of magnesium into the core, so that each magnesium atom will contribute only two electrons (those in the valence $3s$ orbital) to the valence space. This reduces the number of KS equations to be solved from $12N$ to $2N$ for a neutral cluster with N atoms, which obviously amounts to substantially reduce the computational cost.

In addition, the pseudopotential approximation reduces the computational expense for a different reason. It is important to remember that valence electrons can penetrate in the core region, and the orthogonality between core and valence orbitals imposes a complex nodal structure to the valence wavefunctions near the nucleus in an AE calculation. For example, in the case of Mg the $3s$ orbital must be orthogonal to the inner $2s$ and $1s$ orbitals. The oscillations of the valence orbitals in the core region would also increase the computational expense due to the necessity of a very fine discrete grid to accurately represent the valence function in that region.

However, the $3s$ orbital becomes the ground state orbital of the Mg "pseudoatom" in a pseudopotential calculation, and as such it does not have to be orthogonal to other states of lower energy. The resulting pseudo-orbitals are then nodeless and, as we will show, can be chosen to be smooth functions. Pseudopotential theory then elliminates not only the core electrons, but also the oscillations of the valence functions in the core region, further accelerating numerical calculations.

Construction of pseudopotentials

The PP is generated by performing AE calculations on a reference system, in this case, an isolated Mg atom. Different recipes exist to extract a pseudopotential from the AE calculations, depending on specific auxiliary conditions that one wants to impose on the PP. These conditions invariably try to offer a good compromise between accuracy and computational expense. The accuracy is determined by the ability of the PP to describe the physical properties of Mg in arbitrary environments which are different from those employed in the reference calculations, a property called transferability. On the other hand, a PP is computationally "cheaper" the smoother its spatial dependence. And usually smoothness and transferability are competing factors, i.e. improving one of them makes the other worse, hence the need for a compromise.

Now, let's describe the conditions imposed onto our pseudopotentials. First of all, the size

of the core region is defined by the user specifying a radial cutoff (r_c) which sets the boundary that separates the core ($r < r_c$) from the valence region ($r > r_c$). The choice of the core radius is one of the degrees of freedom the user has when constructing a pseudopotential.

The first reasonable condition is that the radial pseudo-wavefunctions (with angular momentum l) generated from the PP must be identical to the AE wave function in the valence region:

$$R_l^{PP}(r) = R_l^{AE}(r) \quad \forall r > r_c \tag{23}$$

Secondly, we impose the equality of the eigenvalues obtained from both calculations, either AE or PP:

$$\epsilon_l^{AE} = \epsilon_l^{PP} \tag{24}$$

In third place, let us call "pseudization region" to the core interval. In our PP method, the pseudo-wavefunction within this region must satisfy a norm conservation condition, resulting in the so-called "norm-conserving pseudopotentials". In words, the charge enclosed within the pseudization region ($0 < r < r_c$) must be equal for the pseudo-wavefunction and the AE wavefunction:

$$\int_0^{r_c} dr |R_l^{PP}(r)|^2 r^2 = \int_0^{r_c} dr |R_l^{AE}(r)|^2 r^2 \tag{25}$$

This restriction ensures the correct shielding of nuclear charge provided by the true core electrons.

Notice that the first and third conditions together do not completely fix yet the radial shape of the pseudo-wavefunction inside the core region, so this is an additional degree of freedom left to the user. This is exploited as to produce a smooth pseudo-wavefunction within $r < r_c$. Other than these purely practical requirements, the pseudo-wavefunction in the core region is "invented" by the user.

In our work the pseudo-wavefunction in the core region is chosen as a smooth and nodeless polynomial [12]. Moreover, it is enforced to be continuous at $r = r_c$ and to have continuous derivatives of up to sixth order at that point. This ensures that the pseudopotential itself is continuous, and intends to generate a smooth PP without very high Fourier components, which is very advantageous to reduce the computational cost.

Once a pseudo-wavefunction satisfying conditions 1 and 3 is designed for each angular momentum channel l, it is inserted into the corresponding KS equation, together with the AE correct eigenvalue (to satisfy condition 2). As the pseudo-wavefunction is nodeless, the KS equation can be inverted to obtain the pseudopotential. However, the PP obtained at this point (called a screened pseudopotential), is not yet ready to be used in molecular calculations, as it still contains the screening effects of all the electrons, including the valence ones. And we want to describe all effects of valence electrons explicitly in the molecular calculation.

Therefore, in a last step we must produce the unscreened PP that will be finally used in the molecular calculations. To unscreen the PP, we must subtract from the screened PP the Hartree and exchange-correlation terms for valence electrons, as those are part of the valence self-consistent space and so should not be part of the external potential!

The total density can be written as the sum of the core and valence densities:

$$n = n_c + n_v \tag{26}$$

The Hartree functional is linear in the density, so there is no problem with the unscreening procedure on that part, as

$$E_H[n] = E_H[n_c] + E_H[n_v], \tag{27}$$

one can subtract $E_H[n_v]$ from the screened PP without any problem. However, problems may appear due to the possible non-linearity of the exchange-correlation term. The LDA functional, for example, is clearly linear, but the GGA which we use in this work is not:

$$E_{xc}[n_c + n_v] \neq E_{xc}(n_c) + E_{xc}(n_v). \tag{28}$$

So in our calculation, if we simply subtracted $E_{xc}[n_v]$ from the screened PP, we would be incurring an error. This error becomes bigger the more important the penetration of valence orbitals into the core region, i.e. when n_c and n_v

overlap significantly, which is precisely the case for alkali and alkaline-earth elements as magnesium.

The solution is to introduce so-called non-linear core corrections, which have the virtue of not significantly contributing to the computational cost. In this approach, the whole $E_{xc}[n]$ is subtracted from the screened PP (thus avoiding the non-linearity problems), and so must be incorporated in the molecular calculation. The "trick" is that the core density is also pseudized and stored. The user just has to define a new cutoff region for core pseudization: the pseudo-core density will be equal to the true n_c only beyond that cutoff radius, and a smooth polynomial below the cutoff. The pseudo-core density is frozen in the molecular calculation, as n_c does not belong to the active valence space, so it does not increase the computational cost. It only participates in the calculation of $E_{xc}[n]$: at each step of the Self-Consistent Field (SCF) Method, the fixed and pseudized n_c is added to n_v to get the correct exchange-correlation energy at no additional cost.

To finish this section, we comment about the choice of cutoff radii for the pseudo-wavefunctions. Shorter values result in a higher precision, but also in a harder PP (with higher Fourier components), so in more expensive calculations. Therefore, cutoff radii are chosen as long as possible while compatible with a reasonable accuracy. This is done by testing the PP in atomic calculations on excited configurations (different from the reference one) and requiring an accuracy of at least 1 mRy in the atomic energies. Additional transferability tests involve PP calculations on the dimer Mg_2 and on the crystalline metal, for which accurate calculations and measurements exist that allow to conclude if the PP is accurate.

2.6 Jellium Model

Until now, we have described an accurate first-principles computational technique to solve the complex many-body electronic problem. It is often interesting, however, to check if the *ab initio* results conform to the expectations extracted from simpler phenomenological models. These last models typically invoke more drastic approximations, and offer only a gross description of electronic and/or atomic structure by focusing on a small subset of descriptive variables, but they can often capture relevant systematic trends in the average properties of a physical system. In order to provide an in depth analysis of our computational results, we will compare them to the prediction of a simple jellium model[13], which is explained in this section.

In the *ab initio* description, the effect of the ionic cores is represented by a sum of atom-centered pseudopotentials. In the jellium model, this is substituted by a (much simpler) uniformly charged positive background called Jellium where valence electrons move, similarly to a system of interacting particles enclosed in a "box". The total jellium positive charge is chosen so as to enforce charge neutrality for the global system in the case of neutral clusters, or to reproduce the total charge in the case of cluster ions. Valence electrons, which are considered to be completely delocalised within the jellium, play the leading role regarding clusters stability and their properties, while the jellium background plays a secondary role by defining the size and shape of the confinement regions.

This model provides a first rough insight into cluster properties, in particular, into the electronic structure which is calculated using the same DFT approximations as in the *ab initio* approach. The jellium model is particularly useful in metallic systems where valence electrons are delocalized.

As in the *ab initio* method described earlier, the expression of the energy ($E[n]$) must be considered; in this case, the external potential is replaced by the so-called jellium potential $V_J[n]$. This potential is defined as the one produced by the jellium background onto valence electrons. The other terms in the energy expression are the same as before: kinetic energy ($T_s[n]$), the Hartree potential ($V_H[n]$), and the exchange and

correlation ($E_{xc}[n]$) potential:

$$E[n] = T_s[n] + V_J[n] + V_H[n] + E_{xc}[n], \quad (29)$$

Although this energy expression is admittedly very simplified, it can produce quite realistic results for physical systems that satisfy the following conditions: (1) the valence electrons are not tightly bound to a particular nuclear center, but rather become delocalized and able to move across the whole system volume; (2) the pseudopotential strength is low enough so that the detailed nuclear skeleton is just a weak perturbation on top of the structureless jellium background. A system satisfying these conditions is called a nearly-free electron system in condensed matter physics. Alkaline and alkaline earth metals, for instance, tend to meet these conditions to a large degree. However, if electrons are much more localized in space, for instance, in the case of transition metals with d-electrons, these conditions are not met and so this model would be inappropriate.

Different flavors of this jellium idea exist in the literature, depending on the shape of the jellium background to start with; but one can also decide whether such jellium shape is frozen or can self-consistently adapt to the electron cloud. One then refers to spherical, ellipsoidal, deformable, etc., jellium models).

The simplest spherical jellium model (SJM) employs a spherically symmetric background of fixed volume (the volume being determined by the average atom density as an external parameter), and for clusters of simple $sp-$bonded metals produced very satisfactory results. One of their most outstanding predictions, verified by experiment, was the existence of an electronic shell structure akin to the well-known one in atoms, which later led to coining the term "superatom" to refer to those molecular systems with an electronic structure mimicking that of atoms. The bunching of electronic energy levels into degenerate shells is a direct consequence of angular momentum restrictions in quantum mechanics. With a fixed spherical shape, it is the radial dependence of the jellium potential the one that decides the energetic ordering of the different shells.

The shell structure induces oscillations in the evolution of stabilities with cluster size, reminiscent of those well-known in the periodic table of atoms. For example, when the cluster has the precise number of electrons to complete a shell it becomes a very stable cluster; however, upon adding another atom, the new valence electrons must occupy the next higher energy levels, thereby the stability of the cluster is reduced. Those special numbers of electrons are called *magic numbers*, and typically are $N_e = 2, 8, 18, 20, 34, 40, 58, 70, 92, 138 \ldots$, which correspond to the most stable clusters with a spherical shape. At those sizes, there is a large gap between the highest occupied molecular orbital (HOMO) and lowest unoccupied molecular orbital (LUMO).

The orbitals in the SJM are named using a notation very similar to the one employed for atoms, with only two differences: (1) the use of capital instead of lowercase letters to denote the angular momentum l and (2) that the ordinal number "$n = 1$" is employed for the first (nodeless) orbital of each angular momentum channel. As a representative example, the electronic configuration which corresponds to the magic number $N_e = 58$ would be: $1S^2 1P^6 1D^{10} 2S^2 1F^{14} 2P^6 1G^{18}$. These molecular orbitals are filled up in order of increasing energy and respecting Pauli's exclusion principle.

The SJM model was generalized for open-shell systems by developing the ellipsoidal jellium model (EJM), in which quadrupolar distortions (either prolate or oblate) away from a spherical shape are considered. The EJM predicts additional (secondary) magic numbers in between the main magic numbers of the SJM, which are observed as well in the fine structure of experimental mass spectra. Open-shell clusters tend to distort its shape in order to further stabilize the occupied subset of orbitals as compared to a perfect sphere (no problem if the unoccupied ones are destabilized as they do not influence the energy), in agreement with general expectations based on the Jahn-Teller theorem.

The ultimate jelllium model (UJM) allows the shape of the positive background density to

be self-consistently relaxed without restrictions (other than a constant volume, of course). In this approach, the nuclear skeleton finds the optimal shape as desired by the distribution of electronic charge, and one says that ions are slaves to the electrons.

In summary, jellium methods completely ignore the detailed atomic structure, accounting only for the global "shape" of the cluster and using the density of the ions as the only external parameter to determine the volume. Furthermore, it is used to describe the electronic structure of molecules in addition to predicting some of their properties. As our results will show, the jellium model provides a very effective way to rationalize the trends of metallic aggregates such as magnesium, a study that otherwise would become much more expensive due to the high level of detail involved in this type of problem.

III Computational method

The term *ab initio* or first-principles is assigned to computations derived directly from theoretical principles, i.e. information obtained from experimental methods is not used, apart from intrinsic properties such as the mass or the charge of the particles involved. In essence, they are based on solving a fundamental equation. In our study, we have chosen the SIESTA code **SIESTA** in order to solve the KS equations for each fixed set of nuclear coordinates. In this section, we will briefly describe the main computational settings employed in the SIESTA calculations, as well as the method to locate the most stable structure of each cluster.

The SIESTA code assumes the Borh-Oppenheimer approximation, and treats the nuclei as classical point-like particles moving in the potential energy surface obtained by solving the electronic problem. This surface, essential for our study, is a surface of $(3N-6)$ dimensions, one for each vibrational degree of freedom of the aggregate. Our aim, in fact, is to find the absolute minimum on this surface for each separate cluster. However, this goal is not so simple to achieve at *ab initio* level, because there are many local minima on that surface, and sampling the whole surface (to be completely sure that the absolute minimum has been found) implies a huge computational cost.

For the study of clusters at the atomic level, some simplification is then needed to deal with the problem at a manageable cost. Previous research in our group has already produced a database containing thousands of different cluster structures, generated by employing simple empirical potentials and global optimization algorithms which are not part of the present work. In this work, we have chosen to perform conjugate gradients optimizations on several structures extracted from that database. The conjugate gradients method essentially uses the *ab initio* values of the atomic forces to relax the input structure towards the nearest local minimum.

The trial structures selected from the database were chosen as those known to be particularly stable in previous studies of Zn and Cd aggregates. The main reason for considering the use of these aggregates as structures to be optimized is that both are isovalent to Mg, and experimental results such as mass spectra or ionisation potentials reveal a very similar size evolution for the three different metals, thus we expect their bonding pattern to be similar. After having optimized different input structures for each size, we assign the most stable one as the putative global minimum (GM) structure. The success of our approach will be tested by explicit comparison with experimental results.

Let discuss next the details of the electronic part of the calculations. We employ norm-conserving pseudopotentials, in their Troullier-Martins form **Troullier**, to model the electron-ion interaction. The pseudopotentials have been generated under the the GGA approximation to exchange and correlation effects and incorporate nonlinear core corrections. Two active valence electrons per Mg atom have been considered.

SIESTA uses atomic orbitals with finite support as a basis set to expand the molecular orbitals. Finite support basis functions are strictly zero beyond some cutoff radius. The same set of atomic orbitals is centered around each Mg atom in the cluster. The main advantage of using a localized basis set, as compared to other usual choices such as plane waves, is that the number of basis functions needed to achieve good accuracy is relatively small, thus increasing the efficiency. However, when using this "linear combination of atomic orbitals" (LCAO) approach, one has to carefully optimize the basis set due to the lack of a systematic convergence procedure.

Our basis functions include an angular and a radial part:

$$\varphi(\vec{r}) = R(r)Y_l^m(\theta, \phi) \tag{30}$$

The angular part is provided by the spherical harmonics, which are implemented within the SIESTA code up to angular momentum quantum numbers of $l = 4$. Although in the magnesium aton only $l = 0$ orbitals are occupied, in order to increase the angular flexibility of the basis we also include so-called polarization orbitals, i.e. orbitals with $l > 0$. The inclusion of $3p$ orbitals into the basis set is essential for the correct description of polarization $sp-$hybridization effects. But we additionally include $l = 2$ orbitals in order to have a very accurate basis.

The finite support radial functions ($R(r)$) are generated in the SIESTA code by performing calculations on an atom confined by an infinite barrier potential, so that the function is exactly zero at the box edge. As the number of radial basis functions centered around each atom increases, a higher radial flexibility is achieved in the variational calculation. In this work, we have employed a basis set of DZP (double-zeta plus polarization) quality, amounting to two s basis functions, six p basis functions, and 10 d basis functions, per Mg atom.

The full details about the pseudopotential, basis set, simulation conditions and initial cluster geometry are provided in two input files with the extensions .psf (pseudopotential formatted), .fdf (flexible data format). The psf file contains the pseudopotentials, one for each angular momentum channel, as numerical functions expressed in a radial grid. It also contains the pseudized core density in case non-linear core corrections are applied. The file is written by the auxiliary *atom* code used to generate the pseudo, and must be read by SIESTA code.

The fdf file contains the description of the basis set, of the initial atom coordinates, and of all the simulation parameters. SIESTA is a big code with many different possible keywords, which are described at length in the user manual; here we focus on the few relevant parameters which are essential in our calculations. In the fdf file, we specify, for example, the system charge ($q = -1$ in our case of magnesium cluster anions), the chosen exchange and correlation functional (GGA), and the simulation method (in our case structure optimization with conjugate gradients method). We additionally specify the convergence criteria: we consider a structure relaxed when all atomic forces are below 0.01 eV/Angstrom). One of the fdf files we used in this work is attached as an example in appendix A.

SIESTA also produces many different output files, and we focus here on those which are most useful for our specific goals. The converged atomic coordinates are written to a file with extension .xyz for direct visualization using computer graphics applications, and also to a .XV file with a higher numerical precision. A file with extension .EIG contains the molecular orbital eigenvalues, which we will use in the discussion of photoemission spectra and metallicity. Finally, in the main output file one can find the cluster energies, which we will use to calculate dissociation energies and discuss cluster stabilities in connection with experimental mass spectra.

IV Results and Discussion

1 Putative GM structures

The putative Global Minimum structures that emerge from our study are shown in Figures 1-2. These results have been contrasted with different studies provided in the bibliography [4], but those do not cover all the sizes that have been studied in our work. The most complete study of anionic magnesium clusters structures covered the range $N = 2 - 22$ using gradient-corrected density functional theory[4] and those results were successfully reproduced in our previous studies [7]. However, for bigger sizes, there are no previous computational results to compare with.

Fig. 1 shows clusters with $N = 3 - 21$ atoms. An equilateral triangular structure is obtained for Mg_3^-. For Mg_4^-, the GM structure changes to a three dimensional form, namely a regular tetrahedron. The growth evolution of the next aggregates is based on different combinations of tetrahedral units: $N = 5$ is formed by two tetrahedral units sharing a face (a trigonal bi-pyramid); $N = 6$ by two tetrahedral units joined by an edge; and Mg_7^- is a slightly distorted pentagonal bi-pyramid, containing five tetrahedral units.

Mg_8^- adopts a deltahedral structure in the form of a snub disphenoid or bisdisphenoid. The GM of $N = 9$ is a tri-capped trigonal prism (TTP), and it becomes a stable substrate for the growth of the majority of anion structures in the size range $N = 10 - 15$, which are based on adding atoms to that TTP unit. Mg_{15}^-, in particular, is obtained by gluing two TTP units together in such a way that three atoms are common to the two units. Mg_{16}^- adopts a bi-layer structure with a chiral C_3 point-group symmetry.

In the small size range $N = 3 - 16$, all the atoms still belong to the cluster surface, with $N = 17$ being the smallest structure that has an internal core atom; furthermore, Mg_{17}^- is a compact structure with a high symmetry: its point group is almost D_{4h} although there is a slight square-to-rhombus distortion that lowers the symmetry down to C_{2v}. Mg_{18}^- and Mg_{19}^- are based on a 13-atom decahedron with adatoms along the equatorial region; some of those adatoms undergo a significant inwards relaxation. The GM structure for $N = 20$ displays a chiral shell with C_3 symmetry surrounding the internal atom. The structure can be viewed as a twisted pyramid as its global shape is clearly pyramidal. Finally, the GM structure for Mg_{21}^- belongs to the same decahedral family observed for sizes $N = 18 - 19$.

Fig. 2 shows clusters with $N = 22 - 38$ atoms. For sizes $N = 22$ and $N = 23$ we still obtain GM structures with a single core atom, and based on a distorted decahedral packing. However, the nearly degenerate isomer of Mg_{23}^- already has 3 core atoms organized linearly, in this case the cluster grows by adding atoms to the core rather than the shell.

With few exceptions, clusters with an internal dimer are clearly favored in the size range $N = 24 - 28$. These clusters have an elongated (prolate) global shape and keep growing by accommodating new atoms at the shell. As an interesting exception, Mg_{25}^- has a nearly degenerate isomer structure which contains a single core atom, whose special stability we ascribe to the very compact and symmetric shell. Mg_{27}^- and Mg_{28}^- can be classified as filled tubular structures. Specially interesting is the highly symmetric C_{6v} tube obtained for Mg_{28}^-. The shell of this tube contains four hexagonal rings stacked with an anti-prism sequence. The tube misses one capping atom, so the structure would be complete for 29 atoms and would have D_{6d} symmetry. The coordination polyhedron around each of the two core atoms is the Z14 Frank-Kasper polyhedron, quite commonly found in intermetallic alloy crystalline phases.

The perfect structure with two complete Z14 units is not the GM structure for Mg_{29}^-, however, because clusters in the size range $N = 29 - 32$ prefer a core with three core atoms in a triangular arrangement, which makes these clusters to have an oblate global shape. The local coordination polyhedron around each core atoms contains 13 nearest neighbors and can

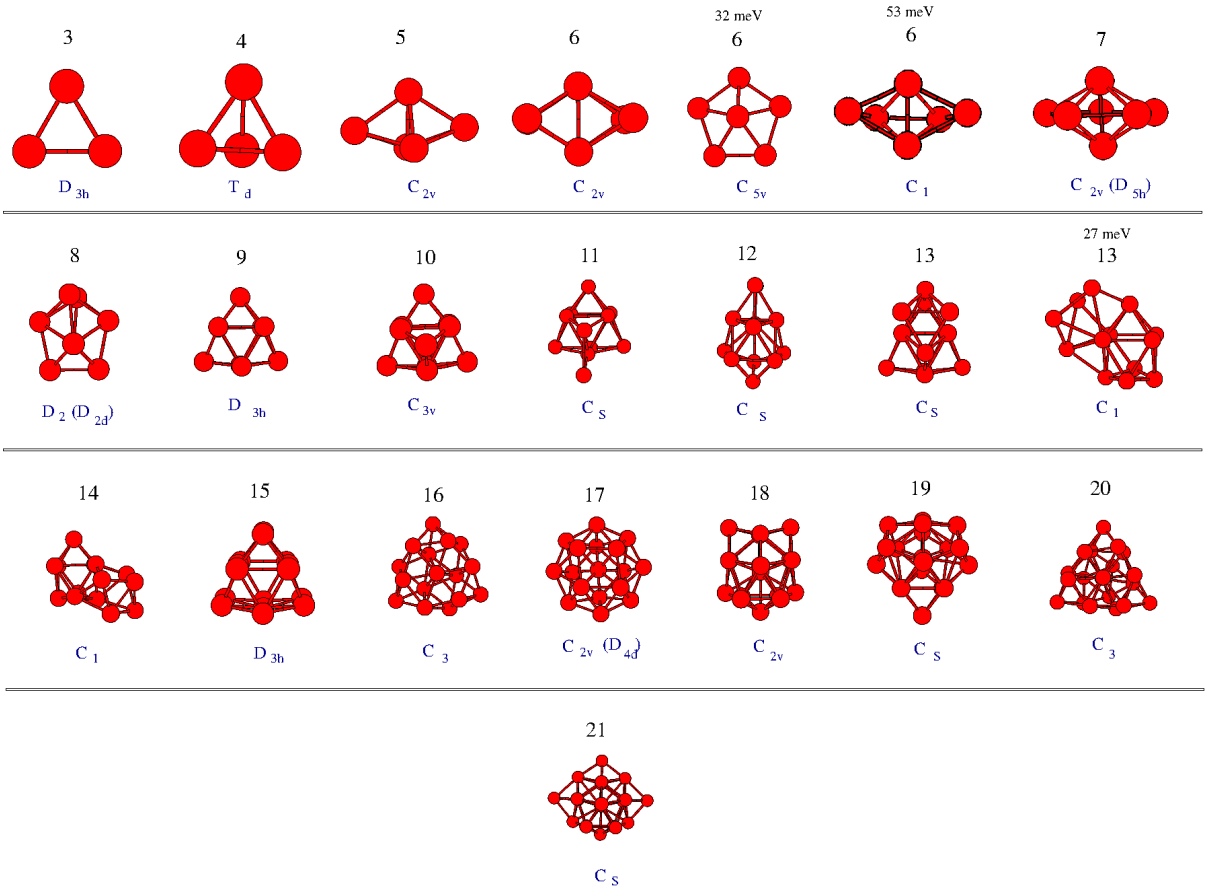

Figure 1: Putative GM structures and approximate point group symmetries of Mg_N^- with $N = 3 - 20$ [7]. Competitive isomers are also shown together with their energy difference with respect to the GM isomer.

not be identified with any of the well-known regular polyhedra, yet most of these clusters maintain a high symmetry (C_{3v} for sizes $N = 30$ and 31). It is also interesting that the growth of the shell around the core is of Janus type, i.e. completely different on the two sides of the core triangle: on one side the growth follows a simple hexagonal stacking, which is not a compact packing; meanwhile, on the other side of the triangle the growth follows and hcp-type compact stacking. Clusters with $N = 33 - 37$ feature a tetrahedral 4-atom core, which equips these clusters with a more spherical shape. The way in which the shell grows around this core is highly dependent on the number of atoms. In particular, the shell of Mg_{34}^- preserves a high chiral C_3 symmetry for the whole cluster. Clusters with $N = 36 - 37$ atoms rather belong to the distorted decahedral family, which has been observed to be stable for Zn and Al clusters as well. Finally, Mg_{38}^- already contains five core atoms in a trigonal bi-pyramidal arrangement, but its shell is quite amorphous and does not preserve any of the symmetries of the core. This is the aggregate with the highest number of core atoms that has been studied in this work.

The study of charged aggregates is motivated by the convenience to compare our computational results with experimental mass spectroscopy data. These experiments need to employ charged clusters for mass selection of

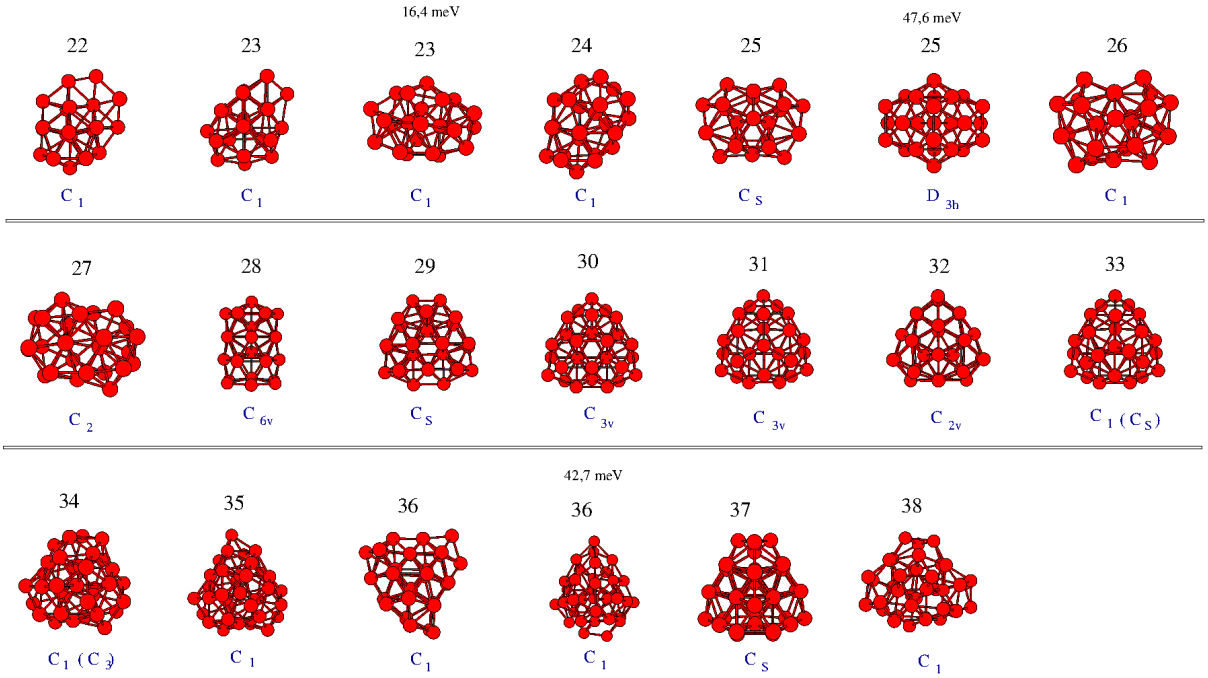

Figure 2: Putative GM structures and approximate point group symmetries of Mg_N^- with $N = 22 - 38$. Competitive isomers are also shown together with their energy difference with respect to the GM.

certain sizes and thus study several physical properties as a function of the number of atoms N. This we will do in the next subsections.

2 Mass spectrometry

All physical and chemical properties of a metallic cluster depend on its atomic and electronic structure. Determining its putative GM structure is the first essential step for a proper characterization of cluster properties at low temperatures. In this work, we focus on studying the energetic stability and electronic properties of the negatively charged magnesium aggregates. In order to achieve a direct connection between experimental and computational results, we will consider the relative abundances measured in mass spectroscopy experiments. Moreover, these measurements are related to the thermodynamic stability of the aggregates. Before we do any comparison, we briefly describe the experimental procedure that was used in the work that we have been taken as a comparative reference [14].

2.1 Mass spectrometry experiments

Magnesium is an element that is usually found in nature forming compounds with other elements. Therefore, it is necessary to use a source that provides isolated, pure magnesium aggregates. Typically, laser ablation of a solid surface is used to generate an atomic magnesium vapour at a very high temperature. Then, an atomic beam of this vapour is guided into a condensation chamber, where there is a very cold and nonreactive gas. Through collisions with the buffer inert gas atoms, the Mg vapor is thermalized at a low temperature so that aggregation events trigger the formation of clusters with a certain mass distribution. The mean size of the cluster distribution can be controlled by tuning external parameters such as the pressure and temperature of the buffer gas, or the length of the collision tube. Under typical operating conditions, the clusters grow via sequential ad-

sorption of individual Mg atoms from the vapor onto pre-existing cluster seeds, and coalescence events between two formed clusters are much less frequent. It is in the condensation chamber that the equilibrium relative abundances are settled. Briefly stated, each time a cluster adsorbs a new atom, it is severely heated by an amount proportional to the adsorption energy. With adsorption energies around 1 eV, the heating is enough to melt the cluster and can lead to evaporation of atoms to release the excess energy (unless collisions with the buffer atoms cool down the cluster before an evaporation event). As clusters of different sizes have different stabilities, those sizes with an enhanced stability will evaporate at a lower rate and thus will become more abundant in the sample. This enhanced stability of certain clusters can be caused either by geometric packing of the atoms or by electronic shell effects. But either way, abundance population of a given cluster size is directly proportional to its stability.

Subsequently, the aggregates are ionized with a laser located at the exit of the condensation chamber, if one wants to study cluster cations; or they become negatively charged by immersing them into an electron bath, if one wants to study cluster anions. Charging is important because aggregates with different mass will follow different paths in a magnetic field, so that the desired size can be selected to study cluster properties as a function of size.

In short, mass spectrometry is a technique that determines the distribution of molecules of a substance as a function of its mass, i.e. its size. However, it is necessary that the particles are charged so that they can be guided efficiently by the magnetic field.

What we have explained is the operation of a typical experimental setup. The experimental results [14] specifically used as reference in this work include some interesting improvements over the typical setup. Magnesium cluster anions were produced by magnetron sputtering using an additional discharge ring at the end of aggregation tube. The discharge produced by the ring efficiently ionizes most of the neutral clusters, except the very small ones that were produced using a laser ablation technique. Clusters produced in the aggregation source and later ionized were stored in a liquid nitrogen cooled ion trap, therefore their temperature is estimated to be as low as 100 K.

Finally, we emphasize that this type of experiments work with aggregates or molecules in gas phase, and the low density of the gas allows the extraction of properties corresponding to an isolated molecule. Each of the aggregates, considered as an independent system, is "in its solid phase" (i.e. with a well-defined geometry) at a sufficiently low temperature.

2.2 Cluster stability indicators

The stability analysis of Mg_N^- clusters is carried out with three indicators that are shown in Figure 6: from top to bottom, these are the binding energy, the evaporation energy and the second energy difference, all three as a function of cluster size.

The first measure is the cohesive energy or binding energy per atom. This global stability measure quantifies the stability of the aggregate with respect to its total dissociation into atoms.

$$E_{\text{cohesive}}(N) = \frac{(N-1)E_1 + E_1^- - E_N^-}{N}, \quad (31)$$

where E_N^- is the total energy of the cluster anion Mg_N^-, E_1 is the energy of a Mg atom, and E_1^- that of a Mg^- anion. The more stable clusters will have higher values of cohesive energy due to the larger energy needed to dissociate them.

The evaporation energy is defined as the energy required to pull out an atom from the cluster. This, in contrast to the previous one, is a local stability measure, as it compares the stability of two aggregates of consecutive sizes:

$$E_{\text{evap}}(N) = (E_1 + E_{N-1}^-) - E_N^-,$$

Finally, the second energy difference compares the stability of a given cluster against the average stability of its two neighbouring sizes:

$$\triangle_2(N) = E_{N+1} + E_{N-1} - 2E_N = E_{\text{evap}}(N) - E_{\text{evap}}(N+1).$$

This parameter is considered the most reliable one of the three magnitudes for a direct comparison with the relative abundances in mass spectra, as it well captures the delicate balance that produces the experimental abundances: in effect, the population of a given cluster size N is expected to increase when: (1) the Mg_N^- cluster has a large evaporation energy; (2) the Mg_{N+1}^- cluster has a low evaporation energy. A positive value of $\triangle_2(N)$ indicates that the population of size N increases by evaporations from size $(N+1)$ at a faster rate than it decays towards size $(N-1)$. Therefore, the most abundant sizes in the experiment should correlate with positive values of $\triangle_2(N)$.

The enhanced abundances of certain cluster sizes in mass spectra can usually be explained by two different factors: the first factor may be a high stability due to a geometric shell closing. These clusters have compact structures, without structural defects such as vacancies or adatoms in their outermost atomic shell, and with a high average coordination number. Adding an atom to these structures necessarily opens up a new geometric shell, reducing their stability by the presence of this so-called adatom, which is easily evaporated. Similarly, removing one atom generates a vacancy defect on the outermost shell and the atoms around the vacancy also evaporate more easily due to their reduced coordination.

The second factor is operative in clusters formed by metallic elements, which have delocalized electrons. These clusters tend to be very stable at an electronic shell closing. This effect will be elaborated later on when we discuss electronic properties.

The theoretical results display a smooth increasing trend for the cohesive energy. On top of that global trend, local maxima or at least a large negative curvature are observed at sizes $N = 9, 10, 15, 19, 20, 31, 34$. Nevertheless, the most stable sizes are not clearly observed in the cohesive energy and it is a good idea to complement it with other indicators. The most stable

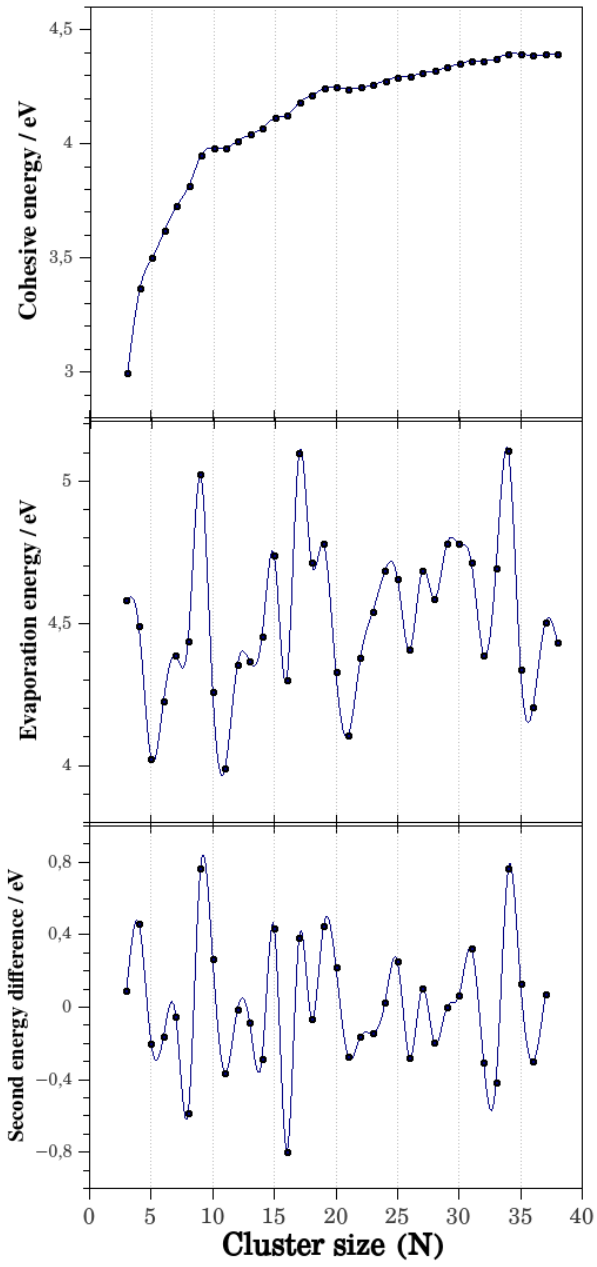

Figure 3: Stability indicators of Mg_N^-: the cohesive energy or binding energy per atom (upper panel), the evaporation energy (middle graph) and the second total energy difference (lower panel).

aggregates against dissociation of one atom are $N = 3-4, 9, 15, 17, 19, 24-25, 27, 29-31$ and 34. Right after these sizes, there is an abrupt decrease in the evaporation energy. Finally, the high and positive values of $\triangle_2(N)$ occur for $N = 4, 9-10, 15, 17, 19-20, 25, 27, 31$ and 34.

The experimental mass spectra have been measured by the group of Bernd von Issendorff at University of Freiburg (Germany), and are freely available in the Thesis of Oleg Kostko[14]. Specifically, mass spectra of Mg_N^- anions can be seen in page 105 of that Thesis. Particularly abundant Mg_N^- clusters are observed for sizes $N = 4, 9-10, 15, 19-20, 25, 27, 29$ and 34, whereas deep minima corresponding to nearly undetectable sizes occur for $N = 11, 21, 26, 28, 32$ and 36. Unusually interesting are the pairs of magic numbers observed for sizes $9-10$ and $19-20$. In both pairs, the smallest cluster (Mg_9^- or Mg_{19}^-) is the most abundant one, but the sharpest population decrease occurs after Mg_{10}^- or Mg_{20}^-.

The theoretical results reproduce the experimental observations almost perfectly. More specifically, we notice that E_{evap} is a more sensitive indicator for the marked maxima in the experimental abundances, while $\triangle_2(N)$ is a more sensitive indicator for the deep minima and globally shows the best agreement with experiment, reproducing in particular the "magic pairs" $9-10$ and $19-20$. The two indicators together provide a nice explanation of the experimental measurements. As a concrete example of their different sensitivities, we mention that sizes $N = 29-31$ are similarly abundant in the experimental spectrum, but with the local maximum located at size $N = 29$. This maximum is captured by the E_{evap} indicator. Meanwhile, the $\triangle_2(N)$ indicator has a local maximum at size $N = 31$ due to the deep abundance minimum at size $N = 32$, i.e. because the sharp abundance decrease is located at size $N = 31$. It is important to realise that the experimental abundances depend on the time that the cluster ions spend on the ion trap, while our theoretical indicators are time-independent. It would be possible to model the evaporation kinetics more precisely using a statistical-mechanical master equation approach, but this is beyond the scope of our work. In any case, our two static indicators are able to explain the experimental results with sufficient accuracy.

The only slight disagreement occurs for sizes $N = 17-18$. In the experimental mass spectra, those two sizes are indeed very abundant (less than Mg_{19}^- but more than Mg_{20}^-). In the theoretical calculations, however, only Mg_{17}^- is found to be very stable, so we believe the failure in our calculations occurs for Mg_{18}^-, whose stability is underestimated. It is possible that we have not located the most stable structure for Mg_{18}^-, or that the level of theory employed is not sufficiently accurate for that size.

Geometric factors clearly contribute to explain the enhanced stabilities for some sizes. For example, the maximum at Mg_4^- correlates with a particularly compact regular tetrahedron structure. Similarly, Mg_9^- has a very compact TTP structure that can be considered a geometric shell closing. Something similar occurs for Mg_{17}^- or Mg_{20}^-, which have compact geometric shell closings without defects. Clusters with low coordinated adatoms, such as Mg_{11}^-, tend to be much less stable. Notwithstanding these trends, we will see later that electronic shell closings are also important in explaining the magic numbers of magnesium clusters. So it is time now to complement these results with an analysis of electronic properties.

3 Electronic properties

Cluster abundances may be essentially determined by two factors. As we have seen until now, geometric shell closing effects related to very compact structures, usually geometries that do not show uncoordinated atoms on their surface, can explain some magic numbers. Another important factor, as we will see in this section, is provided by the electronic shell closing effects that often dominate in small clusters with delocalized valence electrons. The specific sizes at which an electronic shell closing occurs can be predicted using the jellium model[13]: for instance, the spherical model predicts magic numbers when the number of electrons in the aggregate coincides with $N_e = 8, 18, 20, 34, 40, 58, 70, \ldots$. Although it

is known that both factors contribute to the stability of a cluster, it is not easy to deduce if the stability is dominated by geometric or electronic properties, which are moreover interrelated. In most cases, only a combination of both factors can explain the totality of magic numbers.

We will proceed by analysing electronic stability indicators; for this purpose, the ionization potential and the value of the band GAP of magnesium clusters are considered.

Vertical Ionization Potential

The ionization energy is defined as the amount of energy required to remove the least bound electron from the cluster.

Due to the fact that the ionization process may lead to structural changes in the cluster, two types of ionization energies are usually defined: adiabatic and vertical.

The adiabatic ionization energy includes the effects of the structural relaxation that occurs after electron detachment, i.e. it is defined as a total energy difference between local minimum configurations on the potential energy surfaces of anion and neutral clusters, respectively, both in their fundamental vibrational quantum state if zero-point energy corrections are considered (which is not our case). The adiabatic ionization energy of a cluster anion is exactly the same as the adiabatic electron affinity of the neutral cluster. Since we have not optimized in this work the structures of neutral magnesium clusters, we do not have access to the adiabatic ionization energies.

The vertical ionization energy corresponds to the energy difference in a vertical Franck-Condon transition, in which the neutral cluster is left in an excited vibrational state. Due to the very different time scales of electrons and nuclei, this is the quantity most directly accesible in photoemission experiments, as the vertical process has a sizable cross section. It is defined as the energy difference between the anion and the neutral state, both clusters having the optimal geometry of the anion. Notice that it is *not* the same as the vertical electron affinity of the neutral cluster, which would be similarly defined but using the optimal structure of the neutral state. In this work, we have calculated the vertical ionization energies by performing single-point calculations on the neutral charge state at the optimal geometry of the corresponding anion state.

The vertical ionization potential (vIP) of Mg clusters shows variations with cluster size N originated from the delocalized electronic shell structure characteristic of *sp* metal clusters. The electronic shell closings tend to produce local maxima (peaks) in the vIP curves as a function of size. These peaks are usually followed by a sharp drop that indicates the opening of a new electronic shell. The whole picture is very similar to that of atoms in the periodic table.

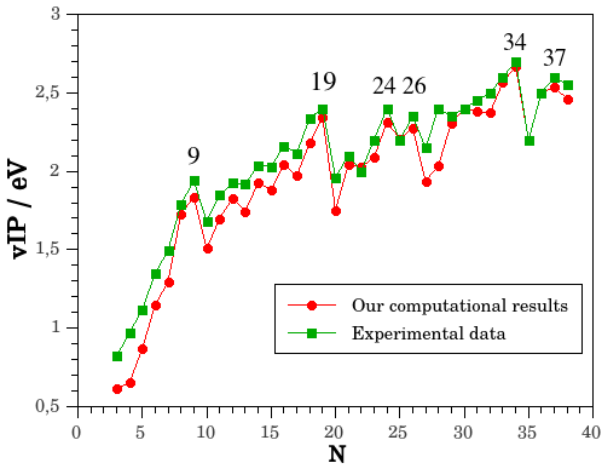

Figure 4: Theoretical values for the vertical ionization potential are compared to experimental results, extracted from Oleg Kostko Thesis[14]

Fig.4 shows experimental measurements of the vIP together with our own results. Most experimental values have been extracted from appendix I of Oleg Kostko thesis[14], but a few ones have been visually estimated from the photoemission spectra reported in appendix F of the same thesis. Due to this visual estimation, those experimental points

may have an inaccuracy of about ±0.05 eV. Despite a small and systematic underestimation of the experimental results, the theoretical results reproduce the experimental trends with an outstanding accuracy, further supporting the whole computational approach. The main discrepancy occurs for size $N = 28$, which suggests that we have not identified the correct global minimum for this particular size. Other than that the agreement is very nice.

Notice that all cluster anions have an odd number of electrons, so none of them can exactly coincide with any of the electron shell closings predicted by the jellium model. Rather, there are pairs of sizes that bracket an electron shell closing. For example, Mg_9^- has 19 valence electrons, and thus is one electron short of the shell closing expected to occur for a system with 20 electrons. Nevertheless, the close proximity of the shell closing induces a local maximum in the vIP. Mg_{10}^- has 21 valence electrons, so its outermost valence electron (i.e. the HOMO orbital) opens a new electronic shell, hence the sharp vIP drop at that size. Similarly, the large drops after sizes $N = 19$ and $N = 34$ correspond to spherical electron shell closings at 40 and 70 electrons, respectively. There are secondary local maxima at $N = 12, 14, 16, 24$. The one for Mg_{16}^- coincides with the spherical shell closing at $N_e = 34$ electrons, the others with subshell closings present in ellipsoidal jellium models, for example at $N_e = 30$ electrons which correlates with the local vIP maximum of Mg_{14}^-. There is a spherical shell closing predicted for $N_e = 58$ electrons, which is seen only in the experimental results as a local maximum for Mg_{28}^-, precisely because this is a size that we fail to assign.

We know that for some sizes geometric factors significantly contribute to explain the enhanced stability. Comparing the vIP results against previous stability indicators of figure 3, we observe that the main vIP maxima at $N = 9, 19$, and 34 correlate with high positive values of Δ_2, so the stability of those clusters has a strong electronic shell closing component. On the contrary, we observe an intriguing regularity for some of the secondary vIP maxima: they are shifted by exactly one size from the local stability maxima. For example, the vIP displays local maxima at $N = 24, 26$ and less important maxima at $N = 14, 16$, while local maxima in Δ_2 occur for $N = 25, 27$ or $N = 15, 17$ respectively. This implies that electronic and geometric effects are competing in those size ranges, with geometric effects being slightly dominant on the thermodynamic stability.

Band gap

Continuing with the electronic study, the so-called "band gap" parameter is now analyzed. Within the context of photoemission experiments on anions, it is defined as the energy difference between the two uppermost occupied states of the anion. As the HOMO of the anion would be unoccupied in the neutral cluster, this parameter loosely corresponds with the HOMO-LUMO gap of the neutral system. However, it is important to realize that the two quantities are not exactly the same: the HOMO-LUMO gap of the neutral cluster should be evaluated at the optimal geometry of the neutral system, while the parameter we quote is evaluated at the optimal geometry of the anion. The following plot shows the variation of the band gap as a function of the size N. The experimental points have been once more estimated from visual inspection of the photoemission spectra, and continue to be accurate only within ±0.05 eV, but this is enough to discern the main trends. For example, due to line broadening, it is difficult to distinguish two energetically close-lying states in the spectra as they may fall under the envelope of a single peak. In those cases we have just set the experimental band gap equal to 0.1 eV.

The figure clearly displays the overall trend of the band gap to gradually shrink as cluster size gets bigger, expected on general grounds for a metallic system. This trend is visible both in experimental and theoretical results. But superimposed to this global trend, there is a series of band gap re-openings that mainly occur at the electron shell closings of the neutral system. They remind us that a definitive establishment of a metallic phase (with zero gap) will only occur at much bigger sizes than studied here.

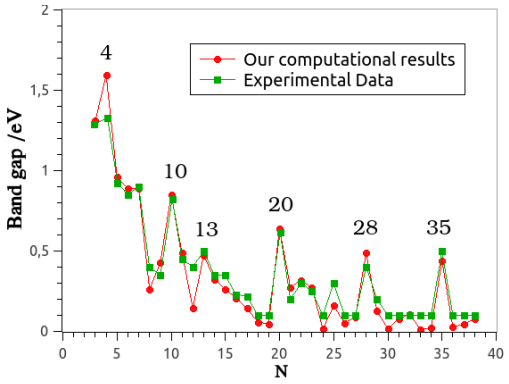

Figure 5: The value of the band gap of magnesium clusters versus cluster size N. Green dots represent experimentally measured values of the band gap by Oleg Kostko[14] and red symbols are our theoretical data.

Our theoretical data are in very good agreement with the experimental data obtained by Kostko[14]. In particular, we reproduce the first significant band gap closing occurring for Mg_{18}^- and Mg_{19}^-, identified in the experimental paper as the smallest Mg particles displaying metallicity. Additionally, there are substantial band gap drops after clusters with $N_e = 8, (14), 20, (26), (30), 34, 40$ and 70 electrons, all of them agreeing with jellium predictions (those in between parenthesis correspond to ellipsoidal predictions, the remaining ones to spherical shell closings). A peculiarity of Mg clusters is the band gap maximum for Mg_{28}, with 56 electrons, as the spherical jellium model predicts this should occur for $N_e = 58$ electrons. It seems that in this local range of sizes geometric effects dominate, because Mg_{29} does not have a spherical shape, but it rather displays a marked oblate distortion, hence it is not strange that it does not display a large gap. Meanwhile, Mg_{28} is strongly prolate so the large band gap might be associated with a subshell closing induced by preferential occupation of superatomic orbitals with low absolute values of the quantum number M, as these are preferentially oriented along the symmetry axis. A tentative valence configuration of $1G^{10}2D^6$ would explain the subshell closing, though a more detailed analysis of the electron density of states of Mg_{28} is needed to extract firm conclusions, which is left for future studies. That our calculations do reproduce the maximum at $N = 28$ suggests that the geometry of Mg_{28}^- is strongly prolate indeed, even if we have not located the correct GM structure.

In conclusion, magnesium clusters clearly exhibit a shrinking gap for small clusters, which closes at certain sizes, with recurrent re-openings at marked electronic shell closings. Thus, magnesium clusters exhibit a relatively early transition from nonmetallic to metallic, but this zero-gap phase can not be considered definitively established. We try to analyze in more depth this gradual evolution towards a metallic state in the next section.

4 Emergence of Metallic Behaviour

Clusters of divalent metallic elements such as the alkaline-earths have become a playground for an analysis of the nonmetal-to-metal transition. In effect, a Mg atom has a non-degenerate ground state, with a fully occupied $3s$ shell and a fully unoccupied $3p$ shell, while bulk Mg is a metallic material with a finite density of states at the Fermi level. As the number of atoms increases, magnesium clusters must transition from a relatively weak bonding between two electronic density distributions rather localized around closed-shell atoms in the dimer, towards a metallic state with delocalized electrons. It is a fundamentally interesting issue to understand how and when this transition occurs.

The following figure shows, in a schematic way employed in many textbooks, the overall evolution of the electronic structure as a function of system size for magnesium clusters:

The figure illustrates how the molecular orbitals generated from the $3s$ and $3p$ atomic orbitals gradually generate the continuous bands of the bulk metal. The overlap between the atomic orbitals increases with size n, both due to a larger number of contacts and also to stronger bonds, and the band width

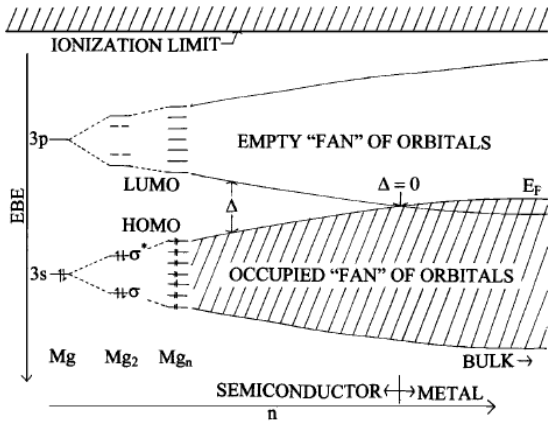

Figure 6

is proportional to the overlap, so the bands widen with size as well. At some point, the completely filled lower-energy band and empty higher-energy band have widened enough to close the gap between them, and the system becomes metallic in the usual sense employed in condensed-matter physics. Before that point, the system would be classified as an insulator or, if the gap is sufficiently small, semiconductor at most. As demonstrated by the experimental works of Freiburg group[14], such a strict closing of the gap can only occur for very large systems, of almost macroscopic scale. Under such a strict definition, none of the clusters here studied could be considered metallic.

Before proceeding, it is important to emphasize that schematic diagrams like this one can produce some confusion if taken too literally. In particular, one should not conclude that the lower-energy band is an "s-band" and the higher-energy band is a "p-band". If only $s-$orbitals were to contribute to the occupied molecular orbitals of small neutral Mg clusters, the "s-band" would be fully occupied, and so all bonding and anti-bonding states derived from the $3s$ orbitals, leading to no net bonding or at most a very weak bonding via dispersion (or van der Waals) interactions, more typical of rare gases. The point is that substantial $sp-$hybridization occurs even in the Mg_2 dimer due to polarization effects and to the fact that the $sp-$excitation energy in a Mg atom is much smaller than the $ps-$excitation energy in rare gases. Thus, both bands in the plot should be considered as $sp-$bands, with the lower one having more contribution from the $3s-$orbitals, the higher one having more contribution from the $3p-$orbitals. Having understood this point, the general picture offered in the figure is equally valid for cluster anions.

It is quite an obvious assertion that the zero-gap condition is incompatible with a system of delocalized electrons (fermions) that is confined to a finite volume of nanometric dimensions. Even the paradigmatic simplest quantum model of metals (the jellium model) develops sizable gaps between highly degenerate electronic shells when confined to a small spherical region, due to general angular momentum conservation restrictions, yet it remains true that the electrons are delocalized across the whole cluster volume. As the zero-gap metallicity criterion is thus impossible to realize in small nanoparticles, we consider more sensible to focus on all other relevant attributes of metallicity, such as electron delocalization or (in the case of alkaline-earths) the extent of $sp-$hybridization, and qualify a nanoparticle as "metallic" (or as metallic as it can possibly be) if it satisfies those alternative criteria. This we will analyze in the next subsection.

Density of states

In this section, we will analyze the electronic density of states (DOS) of a few magnesium clusters to see if they are compatible with the predictions of the jellium model. We will consider an agreement with jellium model predictions as an indirect proof that the electrons are delocalized over the cluster volume. A more detailed analysis would involve an explicit visualization and discussion of the molecular orbitals and a characterization of the topology of the electron density scalar field, which is however beyond the expected scope of this TFM work. We will also study the degree of $sp-$hybridization, which is expected to increase with the cluster size, as a complementary indicator for the gradual evolution towards bulk

metallic properties.

In order to plot the DOS of a given cluster, we just need the Kohn-Sham eigenvalues, which SIESTA code always outputs to a file with extension .EIG. The code can also provide with .DOS and .PDOS files, if asked for them in the input file. The .DOS file contains the density of states in a way that emulates a true experimental measurement (from example from photoemission spectroscopy) by centering a gaussian, of width decided by the user, around each eigenvalue to simulate line broadening. We have decided to apply a broadening of 0.1 eV. The .PDOS file contains more detailed information, namely the contribution of each atomic orbital (basis function) to the total DOS, so that the separate contribution of $s-$ and $p-$orbitals can be obtained and the degree of $sp-$hybridization revealed. The DOS provided by SIESTA is normalized so that its integral up to the Fermi level gives the total number of electrons, thus the area under each peak directly provides the number of electrons contributing to that peak. These figures will be analyzed and we will check if computational results are compatible with the predictions of the jellium models.

As stated before, the peaks in the DOS represent eigenvalues, so if several eigenvalues are degenerate because of the symmetries of the cluster, they will contribute to a single peak. If two eigenvalues are nearly-degenerate, their energies are very close and they can contribute to a single peak depending on the broadening employed. In any case, the area below the peak will always allow us to know the number of electrons it contains.

We mention in passing that a detailed comparison of the theoretical DOS of Mg cluster anions with the photoemission spectra available in Kotko Thesis is one of the most accurate methods for cluster structure assessment. This is so because each different isomer has its own DOS pattern, so that the DOS is an ideal structural fingerprint. This type of analysis would be the natural continuation of our work in future research, but it implies too extensive additional work to include it here.

We will be content here with considering a few specific sizes for the neutral charge state, since the aim of this section is to understand whether the results obtained are compatible with the predictions of jellium models and, for this purpose, it is not necessary to show the results for all sizes. Moreover, considering the neutral state simplifies the analysis because the neutral Mg clusters have no spin polarization, thus producing DOS curves with sharper features for an easier analysis.

As explained in the theoretical section, the notation used to designate molecular orbitals in the spherical jellium model is similar to the one used in atoms, with the difference that capital letters are used instead of lower-case letters and that there are no restrictions on the "principal quantum number" as it is not associated with any observable, and it is used just to distinguish shells with the same angular momentum. The usual Aufbau filling scheme provided by the spherical jellium model is: $1S^2 1P^6 1D^{10} 2S^2 1F^{14} 2P^6 1G^{18} 2D^{10} 3S^2 1H^{22} \ldots$. As in atoms, this is the order observed in most cases, but there may be aggregates with a different filling order since it depends on the shape of the effective radial potential. Moreover, no cluster can have full spherical rotational symmetry even if it has an approximately spherical shape: being formed by a discrete number of point-like nuclei, it will just have one of the point group symmetries. So we do not have to expect all of the essential degeneracies of a sphere; the essential degeneracies will be rather given by the dimensionalities of the irreducible representations of the given point group. But overall it turns out that the spherical jellium pattern of levels is quite well followed if the cluster "shape" is close to spherical. We will use the same notation even for clusters that deviate from sphericity. In these clusters there will be additional fragmentation of angular momentum shells produced by the specific cluster shape.

We will focus on the shell closures and the filling order, as well as the degeneracy breaking resulting from a non-spherical shape of the aggregate. Indeed, we know that the magic

numbers of the spherical model occur for $N_e = 2, 8, 18, 20, 34, 40, 58, 70, \ldots$, but in cases where the splitting within a layer is large enough, new gaps and consequently new magic numbers can be generated, as in ellipsoidal jellium models.

In the next figure we show the DOS of Mg_N clusters for $N = 4, 17, 20, 35$. This way we have a representative selection of sizes covering very small, intermediate size, and the larger sizes addressed in this work. We have explicitly annotated jellium labels on top of each peak or group of peaks.

We will first focus on a discussion of sizes $N = 4, 20$ and 35. This is just because these clusters are approximately spherical at the quadrupolar level (i.e. their three principal inertia moments are quite similar). Meanwhile, Mg_{17} is quite flattened and so has a sizable deviation from sphericity, of oblate character.

The first graph of DOS in fig7 corresponds to the Mg_4 aggregate, which contains 8 valence electrons, and it perfectly agrees with the expected jellium configuration: The lowest-energy peak corresponds to a filled $1S^2$ shell, while the second one integrates to six electrons and so corresponds to the filled $1P^6$ electronic shell. There is a wide HOMO-LUMO gap of around 2 eV as expected from a spherical shell closing configuration. The T_d point symmetry group of this cluster maintains the exact degeneracy within the $1P$ shell. The next peaks are above the Fermi level and so unoccupied. The first one corresponds to the $2S$ orbital, and the other two represent the $1D$, which is fragmented under the tetrahedral symmetry of the nuclear potential. It is interesting to notice that the $2S$ orbital is more stable than $1D$, most probably due to the small size of the cluster and the fact that the $1D$ orbital can be localized on a region external to the cluster, while the $2S$ orbital has at least some weight on the internal region.

Figure 8 shows the DOS of Mg_{20} in its top part. Although this cluster has only C_3 symmetry, its global shape is also tetrahedral, and so quite spherical at the quadrupolar level as expected for a system with 40 valence electrons (we remind the reader that $N_e = 40$ is one of the electronic shell closings in the spherical jellium model). Agreeing with this model, the DOS shows a fair gap at the Fermi level. Moreover, the whole DOS displays a nice match to jellium expectations. The lowest-energy peak corresponds again to $1S^2$ shell. The next peak to $1P^6$. We notice here that the C_3 group at most admits doubly-degenerate irreducible representations, so the $1P_x, 1P_y, 1P_z$ orbitals do not have exactly the same energy in the .EIG file. Nevertheless the cluster shape is spherical enough so that the three levels contribute to a single, slightly wider peak with the employed line broadening employed. The next two peaks correspond to $1D^{10}$, split approximately into two levels containing 6 and 4 electrons. Next peak, $2S^2$, is very close to the $1D$ peak but now following the usual jellium ordering. The next broader band contains 20 electrons and must be associated with $1F^{14}2P^6$ shells. The $1F$ and $2P$ orbitals seem to overlap in energies and it is not possible without further analysis to identify which of those bunched peaks are the $1F$ and which ones are the $2P$, but since the cluster shape has a slightly oblate character, we are quite confident that the HOMO is the $2P_z$ orbital, if we agree to call $z-$axis to the symmetry axis of the inertia ellipsoid. This is because in an oblate object the $2P_z$ orbital overlaps less efficiently with the jellium positive background, which destabilizes that orbital compared to $2P_x, 2P_y$.

Next, we briefly mention that Mg_{35} also conforms to the electronic shell closing predicted at 70 electrons by the spherical jellium model, although the HOMO-LUMO gap is smaller due to the global trend of the gap to decrease with increasing size of the cluster. The several bands, in order of increasing energy, correspond to $1S^2$, $1P^6$, $1D^{10}2S^2$, $1F^{14}2P^6$, $1G^{18}3S^2 2D^{10}$. As before, $1F$ and $2P$ shells overlap in energy space, and now also the $1G, 2D$ and $3S$ shells overlap, so in particular the spherical shell closing expected at an electron count of 58 is only incipient. In summary, we can conclude that Mg clusters with an approximately spherical shape well conform to jellium expectations, as a result of delocalization of the valence electrons.

Finally we consider Mg_{17} as an example of a non-spherical cluster, with a significant oblate character. The first thing we notice is that $N_e = 34$ is a spherical shell closing, i.e. the electrons would like the cluster to adopt

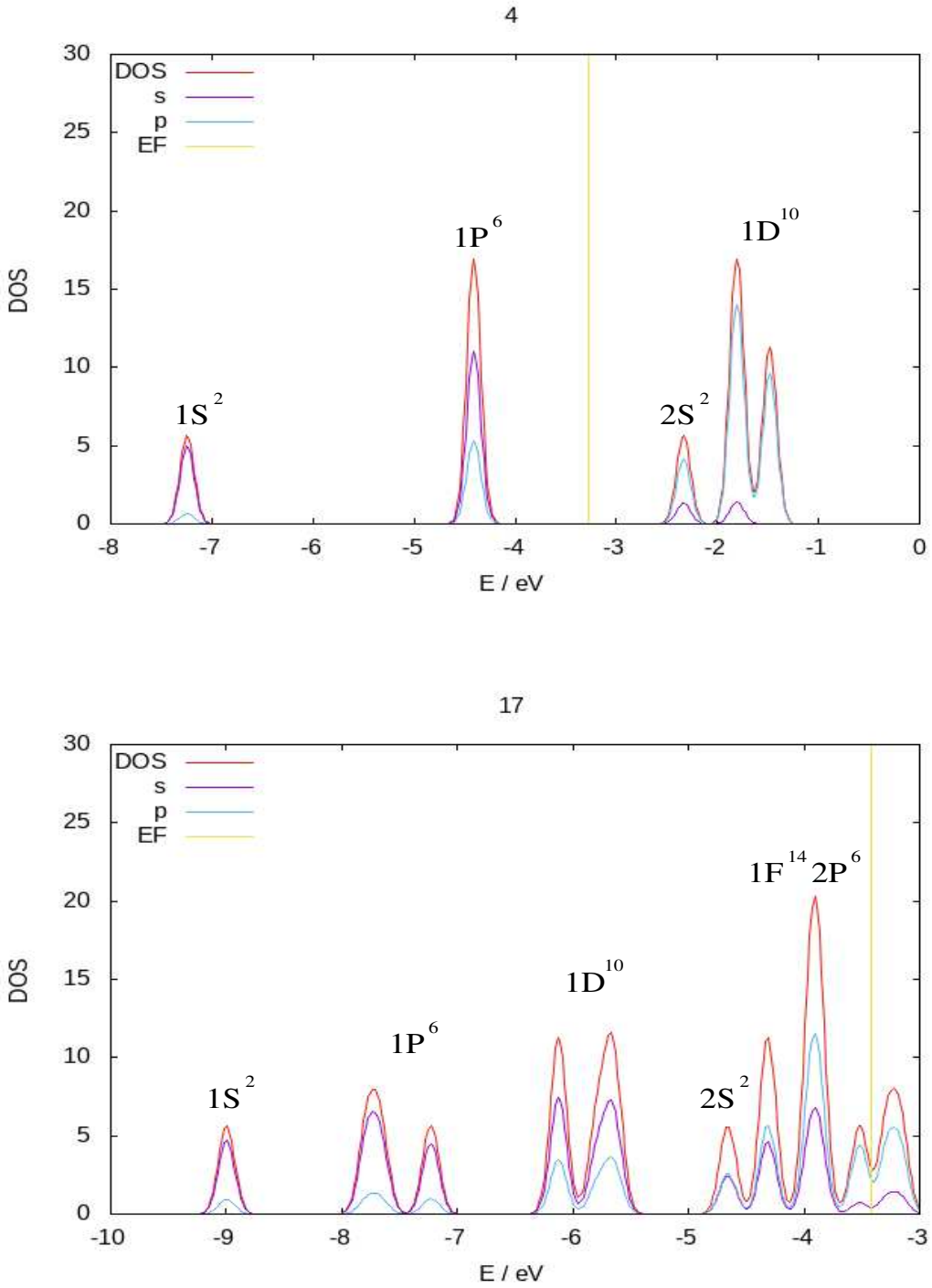

Figure 7: The density of states of Mg_4 and Mg_{17} (red lines) and the separate contributions of $s-$orbitals (purple) and $p-$orbitals (blue) are shown. Also, the Fermi energy (E_F) is shown with a vertical line.

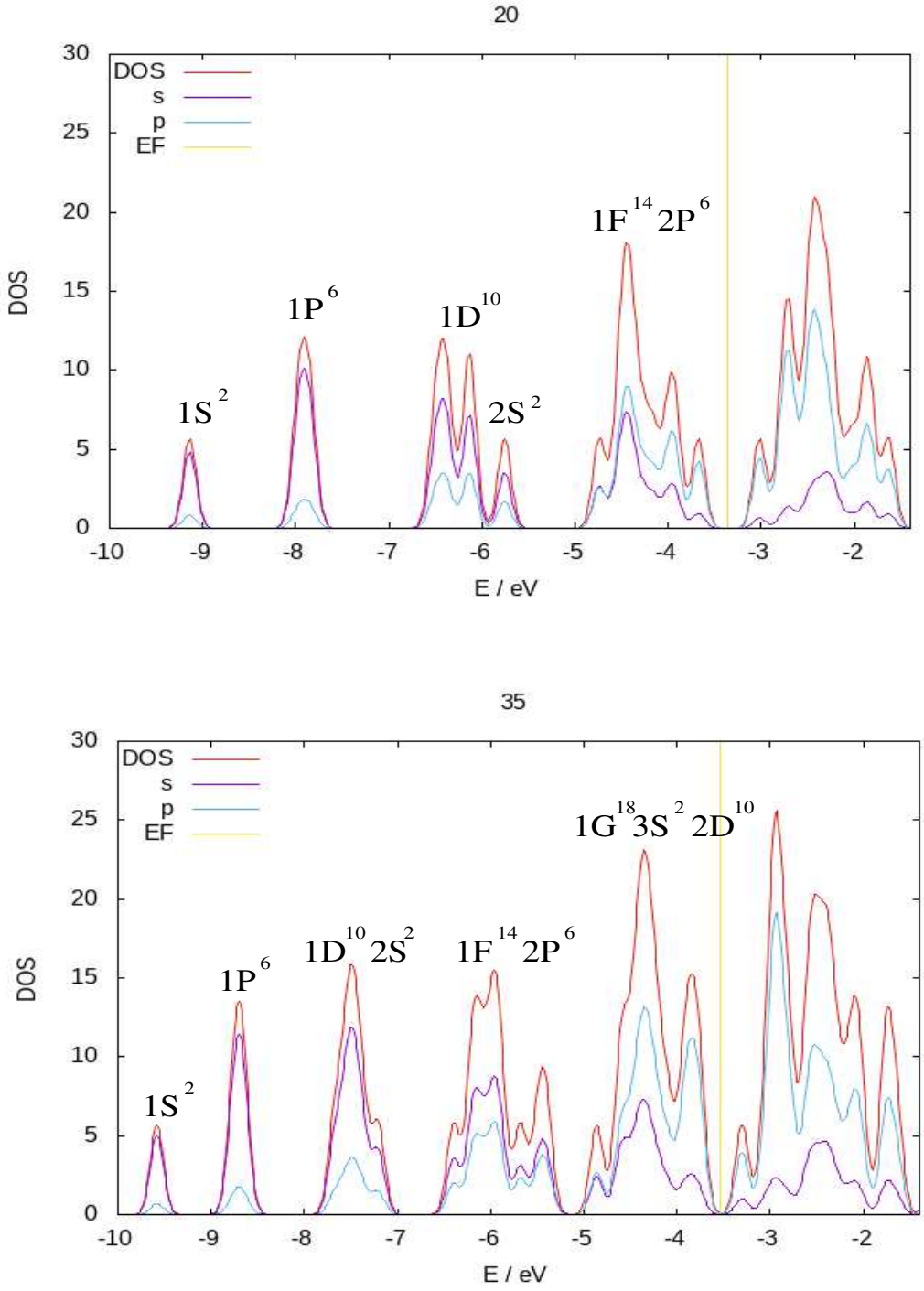

Figure 8: Same information as in the previous figure, but for Mg_{20} and Mg_{35} clusters.

a spherical shape. Failing to observe so is a demonstration that purely geometric packing effects are here dominating over (or at least competing with) electronic shell effects. In fact, the gap at the Fermi level is narrower than expected, and with the broadening employed in plotting the DOS turns into an incipient pseudo gap. Moreover, and although not visible in the figure, the LUMO peak contains four electrons and then there is a sizable gap separating the LUMO from the next peak, so this structure produces a gap at 38 electrons instead of 40 electrons. The oblate distortion is large enough to push the $2P_z$ orbital to high energies and open a gap between $2P_x, 2P_y$ (the LUMO) and $2P_z$, an example of a subshell closing.

Nevertheless, Mg_{17} follows quite well jellium predictions if we account for the effects of the oblate distortion as we have just done, and these effects are, as expected, not so important for the inner orbitals as they don't sample so much the cluster shell region. $1S^2$ is the first peak. The next two ones correspond to the $1P^6$ shell, fragmented into 4+2 electrons as corresponds to an oblate distortion. Notice that the splitting is still large even for such an inner shell, although not so large as for the $2P$ shell. Next two peaks are the $1D^{10}$ shell, split into 4+4+2 electrons although the last 4+2 fall into a single peak with the broadening. $2S^2$ is the next small peak, and the next peaks, as for Mg_{20}, contain a mixture of $1F$ and $2P$ orbitals that we cannot separate.

Concerning the partial density of states contributed by the $3s$ and $3p$ atomic orbitals, a general finding for all cluster sizes is that the deeper molecular orbitals are predominantly formed by $3s$ orbitals, but the percentage contribution of the $3p$ atomic orbitals raises with energy, so the HOMO always has an appreciable contribution from $3p$ atomic orbitals, even in the very small Mg_4 cluster, demonstrating that $sp-$hybridization is an important contributor to the stability of Mg clusters much before the gap is closed. If we focus now on the percentage $3p-$contribution to the HOMO, we see that it increases from approximately 33% in Mg_4 to 55% in Mg_{17}, 66% in Mg_{20} and finally 70% in Mg_{35}. This is already of the same order of magnitude as the $3p-$contribution at the Fermi level of bulk hcp magnesium[15]. In fact it is a little bit larger than the bulk limit value but we have to keep in mind that the cluster structures are still very far from being hcp-like. In any case, it seems that the degree of $sp-$hybridization is already bulk-like even in relatively small Mg clusters, irrespective of the finite gap at the Fermi level.

V Conclusions and summary

Putative GM structures of Mg_N^- with $N = 22 - 38$ atoms have been reported, thus completing our previous study on the smaller sizes $N = 3 - 21$ which was the subject of my TFG work. The complete set of results, including all sizes, has been shown here in order to better appreciate the size-dependent trends. In order to achieve a direct connection between experimental and computational results, we have compared our computational results with experimental data, in particular, with the experimental measurements by the group of Bernd von Issendorff.

Firstly, the cluster abundances of the experimental mass spectral data have been compared with three stability indicators: $E_{\text{cohesive}}(N)$, $E_{\text{evap}}(N)$, and $\triangle_2(N)$. These indicators together provide a nice explanation of the experimental measurements and reproduce the experimental observations almost perfectly: we observed enhanced stabilities for sizes $N = 4, 9 - 10, 15, 19 - 20, 25, 27, 29$ and 34, whereas deep minima corresponding to nearly undetectable sizes occurred for $N = 11, 21, 26, 28, 32$ and 36. E_{evap} is a more sensitive indicator for the marked maxima in the experimental abundances, while $\triangle_2(N)$ is a more sensitive indicator for the deep minima and globally shows the best agreement with experiment.

Geometric and electronic factors contribute to the stability of the clusters, but only a

combination of both factors can explain the totality of magic numbers. As expected for small clusters with delocalized valence electrons, electronic shell closing effects are important in explaining the most marked magic numbers of magnesium clusters.

The vertical ionization potential and the variation of the band gap results are in very good agreement with the experimental data obtained by Kostko. The vIP exhibits variations with cluster size N originated from the delocalized electronic shell structure characteristic of *sp* metal clusters. The main discrepancy occurs for size $N = 28$, which suggests that we have not identified the correct global minimum for this particular size. For the band gap, there are substantial band gap drops after clusters with $N_e = 8, 14, 20, 26, 30, 34, 40$ and 70 electrons, all of them agreeing with jellium predictions. The first significant band gap closing occurs for Mg_{18}^- and Mg_{19}^-, identified in the experimental paper as the smallest size displaying metallicity. So, the studied magnesium clusters clearly exhibit a shrinking gap even for relatively small clusters, which closes at certain sizes, with recurrent re-openings at marked electronic shell closings.

We have additionally checked that our computational results are compatible with the predictions of the jellium models by analyzing the electronic density of states of Mg_N. We focus on the shell closures and the filling order of clusters for $N = 4, 17, 20, 35$ atoms. Taking Mg_{35} as a representative example, it conforms to the electronic shell closing predicted at 70 electrons by the spherical jellium model, although its HOMO-LUMO gap is relatively narrow due to the global trend of the gap to decrease with increasing size of the cluster. Finally, we also show the partial density of states contributed by the $3s$ and $3p$ atomic orbitals and we demonstrate that $sp-$hybridization is an important contributor to the stability of Mg clusters much before the gap is closed.

In summary, we consider this study to be a significant advance and contribution to the cluster field, because it has successfully explained the fundamental properties of Mg aggregates with precision and it has also obtained results capable of reproducing the experimental data as it improves and extends over the previous ones.

References

[1] W. Heer, "The physics of simple metal clusters: Experimental aspects and simple models", *Reviews of Modern Physics*, vol. 65, pp. 611–676, Jul. 1993.

[2] B. Issendorff and O. Cheshnovsky, "Metal to insulator transitions in clusters", *Annual review of physical chemistry*, vol. 56, pp. 549–80, Feb. 2005.

[3] J. Akola, K. Rytkönen, and M. Manninen, "Metallic evolution of small magnesium clusters", *The European Physical Journal D*, vol. 16, pp. 21–24, Jan. 2001.

[4] J. Jellinek and P. Acioli, "Magnesium clusters: Structural and electronic properties and the size-induced nonmetal-to-metal transition", *The Journal of Physical Chemistry A*, vol. 107, Oct. 2002.

[5] P. Acioli and J. Jellinek, "Electron binding energies of anionic magnesium clusters and the nonmetal-to-metal transition", *Physical review letters*, vol. 89, p. 213 402, Dec. 2002. DOI: 10.1103/PhysRevLett.89.213402.

[6] O. Thomas and Zheng, "Onset of metallic behavior in magnesium clusters", *Physical review letters*, p. 213 403, Dec. 2002.

[7] A. Faustino and A. Aguado, "Estudio de primeros principios de las propiedades estructurales y electrónicas de agregados de magnesio", *Universidad de Valladolid. Facultad de Ciencias*, 2019.

[8] M. Brack, "Metal clusters and magic numbers", *Scientific American*, vol. 277, pp. 50–55, 1997. DOI: 10.1038/scientificamerican1297-50.

[9] A. García, "Propiedades estructurales, electrónicas y de transporte de nanoestructuras de baja dimensionalidad", *Universidad de Valladolid, Facultad de Ciencias*, 2010.

[10] R. O. Jones and O. Gunnarsson, "The density functional formalism, its applications and prospects", *Rev. Mod. Phys.*, vol. 61, pp. 689–746, 3 Jul. 1989. [Online]. Available: https://link.aps.org/doi/10.1103/RevModPhys.61.689.

[11] W. Kohn and L. J. Sham, "Self-consistent equations including exchange and correlation effects", *Phys. Rev.*, vol. 140, A1133–A1138, 4A Nov. 1965. DOI: 10.1103/PhysRev.140.A1133. [Online]. Available: https://link.aps.org/doi/10.1103/PhysRev.140.A1133.

[12] N. Troullier and J. L. Martins, "Efficient pseudopotentials for plane-wave calculations", *Phys. Rev. B*, vol. 43, pp. 1993–2006, 3 Jan. 1991. DOI: 10.1103/PhysRevB.43.1993. [Online]. Available: https://link.aps.org/doi/10.1103/PhysRevB.43.1993.

[13] M. Brack, "The physics of simple metal clusters: Self-consistent jellium model and semiclassical approaches", *Rev. Mod. Phys.*, vol. 65, pp. 677–732, 3 Jul. 1993. DOI: 10.1103/RevModPhys.65.677. [Online]. Available: https://link.aps.org/doi/10.1103/RevModPhys.65.677.

[14] O. Kostko, "Photoelectron spectroscopy ofmass-selected sodium, coinage metaland divalent metal cluster anions", *Erlangung des DoktorgradesderFakult at f ur Mathematik und Physikder Albert-Ludwig-Universit at Freiburg im Breisgau*, Feb. 2007. [Online]. Available: https://www.freidok.uni-freiburg.de/fedora/objects/freidok:2964/datastreams/FILE1/content.

[15] A. Junkaew, B. Ham, X. Zhang, A. Talapatra, and R. Arróyave, "Stabilization of bcc mg in thin films at ambient pressure: Experimental evidence and ab initio calculations", *Materials Research Letters*, vol. 1, pp. 161–167, Jun. 2013. DOI: 10.1080/21663831.2013.804218.

VI Appendix

1 A: fdf (flexible data format) file

```
SystemName          Mg22
SystemLabel         Mg22

NumberOfAtoms       22
NumberOfSpecies     1

%block ChemicalSpeciesLabel
 1 12 Mg
%endblock ChemicalSpeciesLabel

PAO.BasisType       split
%block PAO.BasisSizes
 Mg DZP
%endblock PAO.BasisSizes
PAO.EnergyShift     100.0 meV
PAO.SplitNorm       0.15
%block PAO.Basis                # Define Basis set
Mg          3                   # Species label, number of l-shells
 n=3   0   2 P   2                  # n, l, Nzeta, Polarization, NzetaPol
   9.316      6.341
   1.000      1.000
 n=3   1   2                        # n, l, Nzeta, Polarization, NzetaPol
   9.316      6.341
   1.000      1.000
 n=3   2   2
   9.316      6.341
   1.000      1.000
%endblock PAO.Basis
NetCharge           -1
AtomicCoordinatesFormat  Ang
LatticeConstant     30.0 Ang
%block AtomicCoordinatesAndAtomicSpecies < fort.15

XC.functional       GGA
XC.authors          PBE
SpinPolarized       true
FixSpin             true
TotalSpin           1.0

MeshCutoff          180.0 Ry

MaxSCFIterations     200
DM.MixingWeight      0.2
DM.NumberPulay       3
DM.Tolerance         1.d-4


DM.MixingWeight      0.2
DM.NumberPulay       3
DM.Tolerance         1.d-4

SolutionMethod       diagon
DivideAndConquer     true
ElectronicTemperature  200.0 K
#NumberofEigenStates    100

MD.TypeOfRun         CG
MD.NumCGsteps        200
MD.MaxCGDispl         0.1 Bohr
MD.MaxForceTol        0.01 eV/Ang

WriteCoorInitial     true
WriteCoorStep        true
WriteForces          true
WriteDM              true
WriteCoorXmol        true
WriteMDXmol          true
WriteMDHistory       false

UseSaveData
```